FULLY COUPLED FLOW-LIQUEFACTION IN TAILINGS STORAGE FACILITIES: INDUCED SHEAR BANDWIDTH ON PARTIALLY DRAINED TRIGGERS.

NICOLAS A. LABANDA[‡], FELIPE LOPEZ RIVAROLA[∗], NICOLAS TASSO[†], AND VICTOR M. CALO[★]

Abstract. Flow liquefaction remains one of the most critical threats to the stability of Tailings Storage Facilities (TSFs) and its reliable prediction has long been hindered by a fundamental numerical pathology: mesh-dependent localization in computational models. This study demonstrates that fully coupled hydro-mechanical formulations overcome this limitation by embedding pore-pressure diffusion directly into the governing equations, thereby introducing a physically consistent internal length scale absent in uncoupled or purely mechanical approaches. Our spectral analysis derives a dispersion relation governing perturbation growth in the coupled system. Stability emerges when short-wave modes are sufficiently damped—a condition requiring time step increments to exceed a critical threshold. The resulting localization bandwidth is not arbitrary but scales systematically with material and loading parameters: permeability, fluid and skeleton compressibility, and the time step increment expressed as a function of load increment and its rate of application. Thus, the coupled formulation transforms an ill-posed mesh-dependent problem into a well-regularized one via an intrinsic diffusion length scale.

Our numerical simulations span scales from axisymmetric triaxial tests to full TSF configurations, systematically validating our theoretical predictions. Large enough time steps suppress spurious mesh-aligned bands that plague uncoupled models. Reducing permeability—or increasing skeleton compressibility—narrows shear zones and lowers the triggering load for localization, eventually converging to the undrained limit. Load-rate effects follow a predictable pattern: at sufficiently high rates, the system transitions to undrained behavior regardless of permeability, as pore-pressure diffusion becomes negligible compared to loading timescales. We bridge analytical derivations, laboratory-scale validations, and engineering-scale modeling to establish that fully coupled formulations not merely as a numerical convenience but as a rigorous and predictive framework for assessing partially drained liquefaction triggers in tailings dams. We advance both the theoretical understanding of strain localization in fluid-saturated porous media and the practical reliability of safety analyses for critical infrastructure. We clarify the physical mechanisms that control shear band formation under partially drained conditions to provide engineers with a principled basis for evaluating liquefaction susceptibility in TSFs.

Contents

(‡) Principal Tailings Engineer, Mine Waste, WSP, Perth, Australia
(∗) Senior Tailings Engineer, Mine Waste, WSP, Argentina
(†) Tailings Engineer, Mine Waste, WSP, Perth, Australia
(★) Distinguished Professor, Curtin University, Perth, Australia
Date: November 11, 2025.

KEY POINTS

1. Fully coupled hydro-mechanical formulations suppress mesh dependency by embedding a physically consistent internal length scale through pore-pressure diffusion.
2. An analytical equation that describes how material and numerical parameters affect the strain localization bandwidth induced by the fully coupled scheme during flow liquefaction is derived.
3. Spectral analysis shows that stability requires short-wave modes to be damped by increments larger than a critical threshold, linking time stepping directly to localization width.
4. Triaxial simulations confirm this prediction: when Δt exceeds the threshold, shear localization stabilizes into a finite-width band independent of mesh resolution.
5. At TSF scale, permeability, loading rate, fluid and skeleton compressibility and increment size jointly control the onset of liquefaction and the geometry of shear bands, providing a unifying interpretation across scales.
6. Beyond a critical load-rate threshold the response becomes undrained and insensitive to further rate increases; below it, partially drained conditions significantly alter triggering loads.

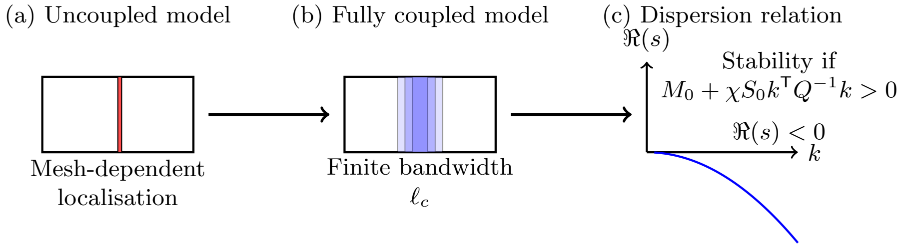

Graphical Abstract. (a) In uncoupled models, localization collapses into single elements, producing mesh-dependent and non-physical results. (b) Fully coupled hydro-mechanical formulations introduce pore-pressure diffusion, which regularizes localization and enforces a finite characteristic bandwidth ℓ_c. (c) The dispersion relation predicts this behavior and provides the scaling law $\ell_c \sim \sqrt{D_{\text{eff}}\,\Delta t}$, consistent with both numerical simulations and analytical derivations.

1. INTRODUCTION

Flow liquefaction remains one of the most critical threats to the safety of tailings storage facilities (TSFs). Even modest disturbances—sudden loads, toe displacements, phreatic surface rises, or water inflows—can trigger runaway failure if the coupled soil–fluid system becomes unstable (Ledesma et al., 2022). Numerical modeling has therefore become indispensable for vulnerability assessment. External actions are progressively applied until failure, enabling safety margins to be quantified (Rógenes et al., 2024). Interest in such models has intensified following post-mortem assessments of catastrophic TSF failures: Mount Polley (Morgenstern et al., 2015), Cadia (Jefferies et al., 2019), Córrego do Feijão (Brumadinho) (CIMNE/UPC, 2021), and Merriespruit (Mánica et al., 2021) among them.

A central challenge in these simulations is the reliable representation of strain-softening behavior. Constitutive models grounded in classical plasticity theory—HSsmall (Brinkgreve et al., 2020), Nor-Sand (Jefferies and Been, 2016), and other critical-state frameworks—capture stiffness degradation and post-peak weakening effectively (Rivarola and Tasso, 2023; Tasso et al., 2024). Yet their predictive capacity depends critically on the surrounding numerical formulation. Purely mechanical or uncoupled flow–deformation analyses suffer from a fundamental pathology: once ellipticity is lost at the onset of softening, strains localize into zero-thickness bands. The computed response then reflects mesh discretization rather than material behavior (Rudnicki and Rice, 1975a; Vermeer and de Borst, 1984). This mesh dependence renders results non-objective and undermines confidence in safety assessments.

To restore well-posedness, constitutive models must be augmented with an internal length scale that spreads deformation over a finite width. Two broad regularization strategies prevail in geomechanics. *Nonlocal or gradient regularization* replaces the local driving variable—typically plastic strain—with an averaged or gradient-enhanced counterpart, often through a Helmholtz-type equation. The internal length parameter then governs shear-band thickness explicitly (Jirásek and Bažant, 2002; Mühlhaus and Aifantis, 1991). *Viscoplastic regularization* introduces a material time scale so that softening unfolds at finite rates, typically via Perzyna or Duvaut–Lions overstress formulations. This rate dependence diffuses plastic strain temporally and spatially, curbing mesh bias (Perzyna, 1966; Duvaut and Lions, 1976). Complementary approaches include Cosserat and micropolar continua, which embed couple stresses and rotational degrees of freedom, and energy-based (crack-band) regularization that enforces finite dissipation per unit area at the integration-point level (Bažant and Oh, 1983; Mühlhaus and Aifantis, 1991). Although this pathology and its remedies are well established in broader geomechanics (Mánica et al., 2018; Cui et al., 2023; Rødvand et al., 2023), comparatively little attention has been devoted to mesh objectivity within tailings-dam analyses (Sottile et al., 2021; Rivarola and Tasso, 2024). This gap is significant. Tailings often exist in loose, contractive states susceptible to liquefaction, where accurate prediction of triggering loads and failure modes is critical for public safety and environmental protection.

Fully coupled hydro-mechanical formulations offer an alternative path to regularization—one that introduces no ad hoc parameters. By solving displacement and pore-pressure fields simultaneously, the formulation embeds fluid mass balance directly into the governing equations. This introduces diffusion as an intrinsic regularization mechanism. The coupling between pore pressure and volumetric strain causes the fluid phase to act as a buffer: it opposes rapid volumetric changes, diffusing deformation in both time and space. Storage terms and Darcy flux together attenuate short-wavelength perturbations, stabilizing the softening response and improving uniqueness (Coussy, 2003). Physically, the diffusion length scale arises from hydraulic diffusivity—a material property governed by permeability and compressibility—rather than from an externally imposed parameter. The same framework transitions naturally between drained, partially drained, and undrained regimes without invoking ad hoc drainage assumptions, capturing the full spectrum of field loading conditions.

Our goal is to clarify how fully coupled formulations regularize softening instabilities in loose tailings and to establish quantitative relationships between material properties, loading conditions, and localization behavior. Using spectral analysis in Fourier–Laplace space, we derive a dispersion relation that governs perturbation growth in the linearized system. This analysis identifies the parameters controlling the finite localization bandwidth: hydraulic diffusivity (permeability and fluid/skeleton compressibility), loading rate, and constitutive softening rate. Short-wavelength modes are damped when time increments exceed a critical threshold, ensuring that shear bands possess finite, mesh-independent width.

We validate our analytical predictions with numerical simulations performed in `PLAXIS 2D` using the HSsmall constitutive model and a van Genuchten soil-water retention curve. Simulations span two scales: axisymmetric triaxial tests that isolate fundamental mechanisms under controlled boundary conditions, and TSF-scale scenarios that incorporate realistic geometries, loading sequences, and heterogeneities. Triaxial tests reveal how time increment selection influences the emergence of short-wavelength noise in shear-band contours—a signature of inadequate regularization. TSF-scale liquefaction-triggering exercises demonstrate how external load rate, permeability, and skeleton compressibility collectively determine shear-band width and the critical load required to initiate flow liquefaction. As permeability decreases or skeleton compressibility increases, the system transitions progressively toward undrained conditions: shear bands narrow, triggering loads decrease, and mesh dependence vanishes. Load-rate effects follow predictably, with high loading rates suppressing drainage and inducing undrained response regardless of permeability. By linking analytical conditions to numerical evidence across scales, we establish a consistent framework connecting laboratory observations, computational modeling, and field-scale liquefaction behavior. This framework provides engineers with a principled basis for selecting time increments, interpreting shear-band formation, and assessing liquefaction susceptibility in partially drained tailings without relying on nonphysical regularization parameters.

This paper is organized as follows. Section 2 summarizes the governing equations of fully coupled poroelastoplasticity, linearizes them about a critical state, and derives the dispersion relation in Fourier–Laplace space for a general multidimensional setting. Section 3 reduces the equations to one spatial dimension, extracting practical guidelines for fully coupled simulations and providing an estimate of the induced shear-band width that underpins mesh-independent results in partially drained and undrained regimes. Section 4 presents numerical validation: triaxial-test simulations demonstrate the role of time increments in suppressing spurious short-wavelength modes, while TSF-scale liquefaction-triggering exercises reveal how load rate, permeability, and skeleton compressibility govern shear-band evolution and failure initiation. Finally, Section 5 synthesizes findings and discusses implications for current TSF design and stability assessment practice.

2. SPECTRAL STABILITY ANALYSIS OF FULLY COUPLED HYDROMECHANICAL SYSTEMS

The spectral analysis of fully coupled hydromechanical systems reveals the fundamental mechanisms by which pore pressure diffusion stabilizes material response and interacts with strain-softening behavior. We linearize about a homogeneous reference state and perform a normal-mode perturbation analysis, deriving dispersion relations that explain why localization manifests with a finite bandwidth rather than collapsing into arbitrarily thin shear bands. This spectral analysis guides our numerical implementation, particularly for selecting stable time steps and load increments in coupled simulations.

2.1. Governing Equations and Constitutive Framework.

We begin by recalling the governing equations for fully coupled flow–deformation problems, in which the displacement field $\boldsymbol{u}$ and the pore water pressure p serve as the primary unknowns. The framework adopted here follows the general hydro-mechanical formulation described in the `PLAXIS` manual (Brinkgreve et al., 2020), but simplified to exclude thermal effects.

The coupled hydromechanical system begins with fundamental kinematic and stress decomposition. The symmetric strain tensor $\boldsymbol{\varepsilon}(\boldsymbol{u})$ captures deformation kinematics:

$$\boldsymbol{\varepsilon}(\mathbf{u}) = \frac{1}{2}\left(\nabla\mathbf{u} + \nabla^{\mathsf{T}}\mathbf{u}\right), \qquad \varepsilon_v = \text{tr}\,\boldsymbol{\varepsilon}(\mathbf{u}), \tag{1}$$

where ∇ is the spatial gradient, the superscript ^{T} implies transpose, and the trace operator tr sums the diagonal entries of the tensor $\boldsymbol{\varepsilon}(\mathbf{u})$ (i.e., tr $\boldsymbol{\varepsilon} = \varepsilon_{ii}$, where repeated indexes imply summation over the index range). The total stress $\boldsymbol{\sigma}$ decomposes into effective stress $\boldsymbol{\sigma'}$ and pore pressure p contributions:

$$\boldsymbol{\sigma} = \boldsymbol{\sigma'} + \chi p\,\mathbf{I}. \tag{2}$$

Here χ represents Biot's coefficient, linking solid skeleton deformation to pore pressure, ε_v denotes the volumetric strain, and $\mathbf{I}$ the identity tensor.

The governing equations for the quasi-static coupled system comprise two fundamental balances and a flow equation:

$$\nabla\cdot\boldsymbol{\sigma} = -\rho\mathbf{g} \qquad \text{(Momentum balance)} \tag{3}$$

$$M(p)\,\dot{p} - S(p)\,\dot{\varepsilon}_v = \nabla\cdot\mathbf{J}_w \qquad \text{(Mass balance)} \tag{4}$$

$$\mathbf{J}_w = \mathbf{C}_w(S)\left(\nabla p + \rho_w\mathbf{g}\right) \qquad \text{(Darcy flow)} \tag{5}$$

where the storage coefficient becomes

$$M(p) = n\left(S(p)\,\alpha_{wP} - \frac{\partial S}{\partial p}(p)\right), \tag{6}$$

and the hydraulic conductivity tensor is

$$\mathbf{C}_w(S) = \frac{k_{\text{rel}}(S)}{\mu}\,\mathbf{K}_{\text{sat}}. \tag{7}$$

Here, the porosity is n, the pressure dependent degree of saturation is $S(p)$, and the mixture density is $\rho = (1-n)\rho_s + nS\rho_w$, with ρ_s and ρ_w the solid and fluid densities, respectively. Moreover, the water compressibility is denoted α_{wP}, while the fluid flux $\mathbf{J}_w$ follows the Darcy law, $\boldsymbol{K}^{\text{sat}}$ is the saturated permeability tensor, $k^{\text{rel}}(S)$ is the relative permeability derived from the Soil–Water Characteristic Curve (SWCC), and μ is the pore-fluid viscosity. Equation (3) expresses the balance of linear momentum in the porous skeleton, including pore pressure contributions, while (4) enforces mass conservation of the fluid phase. In the special case of full saturation ($S = 1$) and nearly constant compressibility, (4) simplifies to a consolidation-type equation. Coupled with (3), this recovers Terzaghi's one-dimensional consolidation theory as a limiting case. The fully coupled system collapses to a purely mechanical formulation under two extreme assumptions: (i) undrained conditions or (ii) drained conditions. Undrained conditions arise when permeability is negligible or loading is extremely rapid, preventing dissipation of excess pore pressures. Drained conditions occur when permeability is effectively infinite or loading is very slow, allowing instantaneous pore-pressure equilibration. In these limits, $\mathbf{J}_w \approx \mathbf{0}$ or $\partial p/\partial t \approx 0$, and the mass balance, (4), ceases to influence the mechanical response. Thus, thee remaining momentum balance, (3), governs the response, with the pore pressure p interpreted either as a constant undrained pressure field or discarded entirely in dry or drained conditions. This reduction aligns with deformation-only analyses common in engineering practice. *Yet it is precisely in such simplified settings that pathological mesh sensitivity emerges under strain-softening conditions.*

The coupling term in (4) introduces the storage coefficient $M(p)$ which encodes how pore pressure changes affect both fluid compressibility and saturation-dependent storage capacity. In addition, this equation adds a subtle but decisive effect: an effective viscous-like resistance that regularizes the mechanical problem. Because the pore pressure and volumetric strain evolutions are coupled, the fluid phase acts as a buffer against abrupt volumetric changes, diffusing deformation in both time and space. This mechanism delays localization and enforces a finite bandwidth for deformation zones, playing a role analogous to viscosity in fluid mechanics. The storage terms and Darcy flux combine to create an internal damping effect, suppressing short-wavelength perturbations that would otherwise concentrate deformation into vanishingly thin shear bands. Previous theoretical studies have suggested that this additional diffusion equation restores uniqueness in the evolution of the plastic multiplier, thereby regularizing the overall solution (Coussy, 2003). The strength of this regularization, however, depends critically on both material parameters—such as permeability, compressibility, and SWCC characteristics—and numerical aspects, including the chosen time-stepping scheme. Identifying which factors dominate, and how they govern the emergent width of localization zones, remains a central question. Addressing this interplay between material physics and numerical resolution is the focus of this paper.

Elastoplastic Constitutive Response. The effective stress evolves according to elastoplastic theory. In rate form, the constitutive response reads:

$$\dot{\boldsymbol{\sigma}}' = \mathbb{C}^e : \dot{\boldsymbol{\varepsilon}} - \lambda\, \mathbb{C}^e : \mathbf{M}, \tag{8}$$

where $\mathbb{C}^e$ denotes the elastic moduli (stiffness) tensor, $\lambda \geq 0$ is the plastic multiplier, and $\mathbf{M} = \partial G/\partial \boldsymbol{\sigma}$ represents the plastic flow direction derived from potential $G(\boldsymbol{\sigma})$.

Plastic admissibility requires stress states to satisfy $F(\boldsymbol{\sigma}, \kappa) \leq 0$, where F is the yield function and κ represents internal hardening variables. During plastic loading, the consistency condition $\dot{F} = 0$ determines the plastic multiplier through:

$$\lambda = \frac{\mathbf{N} : \mathbb{C}^e : \dot{\boldsymbol{\varepsilon}}}{H + \mathbf{N} : \mathbb{C}^e : \mathbf{M}}, \tag{9}$$

where $\mathbf{N} = \partial F/\partial \boldsymbol{\sigma}$ is the yield surface normal and $H = \partial F/\partial \kappa$ governs the effective hardening ($H > 0$) or effective softening ($H < 0$) behaviour. This framework naturally accommodates both associative plasticity ($F = G$) and non-associative flow ($F \neq G$).

Linearization and Incremental Tangent Operators. We perform the spectral analysis by first linearizing the governing equations around a homogeneous reference state $(\mathbf{u}_0, p_0)$ characterized by rates $(\dot{p}_0, \dot{\varepsilon}_{v0}, \nabla p_0)$. We then introduce the incremental perturbations $(\delta\mathbf{u}, \delta p)$ that represent Newton directions or modal perturbations. Thus, the elastoplastic tangent modulus becomes:

$$\mathbb{C}^{ep} = \frac{\partial \boldsymbol{\sigma}'}{\partial \boldsymbol{\varepsilon}}\Big|_0 = \mathbb{C}^e - \frac{\mathbb{C}^e : \mathbf{M} \otimes \mathbf{N} : \mathbb{C}^e}{H + \mathbf{N} : \mathbb{C}^e : \mathbf{M}}, \tag{10}$$

while hydraulic properties linearize as:

$$M_0 = M(p_0), \quad S_0 = S(p_0), \quad M_p = \frac{dM}{dp}\Big|_{p_0}, \quad S_p = \frac{dS}{dp}\Big|_{p_0}, \tag{11}$$

$$\mathbf{C}_{w0} = \mathbf{C}_w(S_0), \quad \mathbf{C}_w' = \frac{d\mathbf{C}_w}{dS}\Big|_{S_0} = \frac{1}{\mu}\,\mathbf{K}_{\text{sat}}\,\frac{dk_{\text{rel}}}{dS}\Big|_{S_0}. \tag{12}$$

The linearized momentum balance becomes:

$$\nabla \cdot \left(\mathbb{C}^{ep} : \boldsymbol{\varepsilon}(\delta\mathbf{u}) + \chi\, \delta p\, \mathbb{I}\right) = \mathbf{0}, \tag{13}$$

and the linearized mass balance yields:

$$\begin{aligned} &M_0\, \delta\dot{p} + M_p\, \dot{p}_0\, \delta p - S_0\, \delta\dot{\varepsilon}_v - S_p\, \dot{\varepsilon}_{v0}\, \delta p \\ &\quad - \nabla \cdot \left(\mathbf{C}_{w0}\, \nabla \delta p\right) - \nabla \cdot \left(\mathbf{C}_w' S_p\, \delta p\, (\nabla p_0 + \rho_w \mathbf{g})\right) = 0. \end{aligned} \tag{14}$$

Physical Interpretation and Coupling Mechanisms. The linearized (incremental) momentum equation (13) highlights the interplay between mechanical and hydraulic perturbations. Mechanical disturbances propagate through the elastoplastic stiffness tensor $\mathbb{C}^{ep}$, while pore-pressure fluctuations couple to deformation via Biot's coefficient χ. When the hardening modulus $H < 0$, the material exhibits *effective strain-softening* (also referred to as frictional softening), which can destabilize the tangent stiffness and promote localization. Alternatively, *flow* or *static liquefaction* may occur when the plastic flow potential has a negative derivative with respect to the first stress invariant—indicating a contractive material response. The mass incremental balance equation (14) governs how pore pressure evolves under these conditions. The terms $M_0\, \delta\dot{p}$ and $S_0\, \delta\dot{\varepsilon}_v$ represent fluid storage and volumetric coupling between the solid skeleton and the pore fluid. The diffusion term, $\nabla \cdot (\mathbf{C}_{w0}\, \nabla \delta p)$, introduces a stabilizing mechanism: it redistributes pressure gradients in space and time, mitigating abrupt volumetric changes and delaying the onset of localization. The additional terms involving M_p, S_p, and $\mathbf{C}'_w$ capture nonlinear contributions from pressure-dependent storage and saturation-controlled permeability, which become increasingly relevant under partially drained or unsaturated conditions. Together, these terms define the coupled dynamics that govern the initiation, growth, and eventual stabilization of strain-softening instabilities in saturated geomaterials. Thus, this linearized framework forms the foundation for spectral analysis, revealing how diffusion length scales compete with mechanical instability wavelengths to determine the characteristic size of localization phenomena. The interplay between these mechanisms governs whether systems exhibit diffuse deformation, sharp localization, or intermediate band-like structures.

Implications for Numerical Implementation. The spectral structure embedded in equations (13)-(14) guides our discussion. The coupling between mechanical and hydraulic time scales requires careful consideration of temporal discretization schemes. The diffusion-dominated terms suggest explicit time-stepping limitations, while the mechanical coupling may demand implicit treatment of certain terms. Furthermore, the wavelength selection inherent in the spectral analysis provides natural guidelines for the spatial discretization. Elements much smaller than the characteristic diffusion length fail to capture the physics properly, while elements much larger miss essential localization features. Thus, this spectral perspective bridges theoretical understanding with practical computational requirements, ensuring that numerical simulations capture the essential physics of coupled hydromechanical systems.

2.2. Normal-Mode Perturbation Analysis.

We investigate the spectral properties of the linearized system of Section 2.1 by introducing normal-mode perturbations, which capture both spatial and temporal variations. This approach transforms the partial differential equations into algebraic eigenvalue problems, revealing the fundamental wavelengths and growth rates that govern the system's stability.

Fourier-Laplace Transform of Perturbations. We introduce perturbations of Fourier-Laplace type around the homogeneous reference state (Gerolymatou et al., 2024)

$$\{\delta \mathbf{u}, \delta p\} = \{\hat{\mathbf{u}}, \hat{p}\}\, e^{i\mathbf{k}\cdot\mathbf{x}+st}, \tag{15}$$

where $\mathbf{k} \in \mathbb{R}^3$ represents the wave vector with magnitude $k = \|\mathbf{k}\|$, and $s \in \mathfrak{C}$ denotes the complex growth rate. Let $i^2 = -1$. The real part $\Re(s)$ determines the stability of the problem solution: positive values indicate exponential growth leading to instability, while negative values correspond to decay. The imaginary part $\Im(s)$ governs oscillatory behavior, revealing the natural frequencies of the coupled system.

This normal-mode ansatz effectively decomposes the infinite-dimensional dynamical system into a discrete spectrum of modes, each characterized by its wavelength $\lambda = 2\pi/k$ and growth rate s. The physical interpretation is: short wavelengths (large k) correspond to highly localized perturbations, while long wavelengths represent more diffuse deformation patterns.

Transformation of the Momentum Balance. We first evaluate spatial derivatives to substitute the normal-mode ansatz (15) into the linearized momentum balance (13). Thus, the strain tensor for the perturbation becomes:

$$\boldsymbol{\varepsilon}(\delta\mathbf{u}) = \frac{i}{2}(\mathbf{k}\otimes\hat{\mathbf{u}} + \hat{\mathbf{u}}\otimes\mathbf{k})\, e^{i\mathbf{k}\cdot\mathbf{x}+st}, \tag{16}$$

where the factor i arises from spatial differentiation and the tensor product captures the symmetric nature of the strain.

The divergence of the effective stress contribution requires detailed analysis. Using index notation with Einstein summation convention, we have:

$$\varepsilon_{pq}(\delta\mathbf{u}) = \frac{1}{2}(\partial_p \delta u_q + \partial_q \delta u_p) = \frac{i}{2}(k_p \hat{u}_q + k_q \hat{u}_p)\, e^{i\mathbf{k}\cdot\mathbf{x}+st}, \tag{17}$$

$$\sigma'_{mn} = C^{ep}_{mnpq}\varepsilon_{pq}(\delta\mathbf{u}) = C^{ep}_{mnpq}\frac{i}{2}(k_p \hat{u}_q + k_q \hat{u}_p)\, e^{i\mathbf{k}\cdot\mathbf{x}+st}. \tag{18}$$

Taking the divergence and exploiting the minor symmetry $C^{ep}_{mnpq} = C^{ep}_{mnqp}$, which cancels the factor of 1/2, yields:

$$\begin{aligned}[\nabla\cdot(\mathbb{C}^{ep} : \boldsymbol{\varepsilon}(\delta\mathbf{u}))]_n = \partial_m \sigma'_{mn} &= i k_m C^{ep}_{mnpq}\frac{i}{2}(k_p \hat{u}_q + k_q \hat{u}_p)\, e^{i\mathbf{k}\cdot\mathbf{x}+st} \\ &= -C^{ep}_{mnpq} k_m k_p \hat{u}_q\, e^{i\mathbf{k}\cdot\mathbf{x}+st},\end{aligned} \tag{19}$$

where we used $i^2 = -1$ and the symmetry property.

The pressure gradient term transforms more straightforwardly:

$$\nabla \cdot (\chi \delta p \mathbf{I}) = \chi \nabla \delta p = i\chi \mathbf{k} \hat{p}\, e^{i\mathbf{k}\cdot\mathbf{x}+st}. \tag{20}$$

The Acoustic Tensor and Reduced Momentum Equation. Combining equations (19) and (20), the linearized momentum balance reduces to:

$$-C^{ep}_{mnpq} k_m k_p \hat{u}_q + i\chi k_n \hat{p} = 0. \tag{21}$$

since the common exponential factor is non-zero for all combinations of $\mathbf{k}$ & $\mathbf{x}$ and s & t.

We express this algebraic equation compactly by introducing the *acoustic tensor*:

$$Q_{nq}(\mathbf{k}) := C^{ep}_{mnpq} k_m k_p, \tag{22}$$

which encapsulates the directional stiffness properties of the material along the wave vector direction. The momentum balance then becomes:

$$\mathbf{Q}(\mathbf{k})\hat{\mathbf{u}} - i\chi \mathbf{k}\hat{p} = \mathbf{0}. \tag{23}$$

Coupling Structure and System Implications. The reduced momentum balance (23) reveals the fundamental coupling between mechanical deformation and pore pressure in the spectral domain. The term $i\chi\mathbf{k}\hat{p}$ represents how pressure gradients generate body forces that drive displacement perturbations. This coupling term is purely imaginary, indicating a 90° phase shift between pressure gradients and displacement responses. The acoustic tensor $\mathbf{Q}(\mathbf{k})$ determines the mechanical stiffness in each wave direction, while the coupling coefficient χ controls how strongly pressure variations influence the mechanical response. In the limit $\chi \to 0$ (dry conditions), the momentum balance decouples from the pressure, reducing to the purely mechanical eigenvalue problem $\mathbf{Q}(\mathbf{k})\hat{\mathbf{u}} = \mathbf{0}$.

This spectral representation forms the foundation for analyzing the complete coupled system, where the momentum equation (23) must be solved simultaneously with the transformed mass balance to determine the full spectrum of growth rates and corresponding eigenmodes.

Physical and Mathematical Properties of the Acoustic Tensor. The acoustic tensor $\mathbf{Q}(\mathbf{k})$ inherits mechanical properties from the elastoplastic tangent modulus $\mathbb{C}^{ep}$. Writing $\mathbf{k} = k\mathbf{n}$ where $\mathbf{n}$ is the unit wave direction, we obtain:

$$\mathbf{Q}(\mathbf{k}) = k^2(\mathbf{n} \cdot \mathbb{C}^{ep} \cdot \mathbf{n}), \tag{24}$$

revealing that the acoustic tensor scales quadratically with wavenumber and depends on the directional stiffness along $\mathbf{n}$. For stable materials (elastic and hardening), $\mathbf{Q}(\mathbf{k})$ remains positive definite for all $\mathbf{k} \neq \mathbf{0}$. However, during strain-softening (frictional and liquefaction softening), certain components of $\mathbb{C}^{ep}$ may become negative, potentially rendering $\mathbf{Q}(\mathbf{k})$ indefinite for specific wave directions. This loss of positive definiteness signals the onset of localization instabilities. Therefore, the determinant $\det[\mathbf{Q}(\mathbf{k})]$ is a scalar measure of directional stability. When this determinant vanishes for some $\mathbf{k} \neq \mathbf{0}$, the corresponding wave direction becomes neutrally stable, marking the threshold for localization. The eigenvectors of $\mathbf{Q}(\mathbf{k})$ at this threshold define the preferred orientation of emerging localization bands (Rudnicki and Rice, 1975b).

2.3. Mass Balance in Fourier Space.

The transformation of the linearized mass balance equation into Fourier space reveals the intricate interplay between diffusive stabilization, reactive coupling, and advective transport that governs the dynamics of pressure perturbations. Our analysis seeks to elucidate the contributions of various physical mechanisms to the spectral response and determines the characteristic time and length scales of the coupled system.

Fourier Transformation of Mass Balance Terms. Substituting the normal-mode ansatz (15) into the linearized mass balance (14) and canceling the common exponential factor $e^{i\mathbf{k}\cdot\mathbf{x}+st}$ yields:

$$\left(M_0 s + M_p \dot{p}_0 - S_p \dot{\varepsilon}_{v0} + \mathbf{k} \cdot \mathbf{C}_{w0} \cdot \mathbf{k} - i\, S_p\, \mathbf{k} \cdot \mathbf{C}'_w \left(\nabla p_0 + \rho_w \mathbf{g}\right)\right) \hat{p} - S_0\, s\, i\mathbf{k} \cdot \hat{\mathbf{u}} = 0. \tag{25}$$

This expression captures the complete spectral structure of the mass balance, encoding multiple physical processes within a single algebraic constraint. Each term carries distinct physical significance and contributes differently to the overall response of the system.

Operator Decomposition and Physical Interpretation. We seek to illuminate the underlying physics by decomposing the mass balance operator into physically meaningful components. The perturbed mass balance assumes the compact form:

$$A(\mathbf{k}, s)\hat{p} + B(s)i\mathbf{k} \cdot \hat{\mathbf{u}} = 0, \tag{26}$$

where the pressure operator decomposes into reactive, diffusion, and phase-drift terms:

$$A(\mathbf{k}, s) = A_{\text{react}}(s) + A_{\text{diff}}(\mathbf{k}) - iA_{\text{phase}}(\mathbf{k}), \tag{27}$$

and the hydromechanical coupling term is:

$$B(s) = -S_0 s. \tag{28}$$

Each term encapsulates a distinct physical mechanism that governs the system's spectral response.

Reactive Contributions. The reactive term captures time-dependent storage and source effects:

$$A_{\text{react}}(s) = M_0 s + \Pi_0, \quad \Pi_0 = M_p \dot{p}_0 - S_p \dot{\varepsilon}_{v0}. \tag{29}$$

Here, $M_0 s$ represents the fundamental storage response proportional to the growth rate, while Π_0 encodes the nonlinear coupling effects arising from the background loading history. The parameter Π_0 reflects how pressure-dependent storage ($M_p \dot{p}_0$) competes with saturation-induced storage changes ($S_p \dot{\varepsilon}_{v0}$) at the reference state. This competition can either stabilize or destabilize perturbations depending on the loading path and material properties.

Diffusive Stabilization. The diffusion term provides the primary stabilizing mechanism:

$$A_{\text{diff}}(\mathbf{k}) = \mathbf{k} \cdot \mathbf{C}_{w0} \cdot \mathbf{k}. \tag{30}$$

This term encodes a quadratic dependence on wave number that reflects the second-order nature of the diffusion operator. Short-wavelength perturbations (large k) experience strong diffusive damping, while long-wavelength modes remain relatively unaffected by pressure redistribution. The hydraulic conductivity tensor $\mathbf{C}_{w0}$ determines the anisotropy and magnitude of this stabilization process, directly linking the material permeability to the overall system stability.

Phase-Drift Effects. The phase-drift term introduces complexity through advective transport:

$$A_{\text{phase}}(\mathbf{k}) = S_p \mathbf{k} \cdot \mathbf{C}'_w (\nabla p_0 + \rho_w \mathbf{g}). \tag{31}$$

This term arises from the nonlinear dependence of hydraulic conductivity on the saturation and couples the background pressure gradient with the dynamics of the perturbations. The factor

$$\mathbf{C}'_w = \frac{d\mathbf{C}_w}{dS}$$

quantifies how permeability changes with saturation, while the vector $(\nabla p_0 + \rho_w \mathbf{g})$ represents the deviation from hydrostatic equilibrium. Under hydrostatic conditions where $\nabla p_0 + \rho_w \mathbf{g} = \mathbf{0}$, this term vanishes completely, reducing the operator to purely real and diffusive. However, when pressure gradients deviate from hydrostatic balance—as occurs during loading or in the presence of external forces—the phase-drift term introduces imaginary contributions that can shift the frequencies of oscillatory modes and potentially destabilize the system through resonance effects.

Hydromechanical Coupling. The coupling term (28) (i.e., $B(s) = -S_0 s$) links pressure perturbations to volumetric strain rates through the saturation-dependent storage coefficient S_0, a fundamental coupling to poromechanics reflecting how skeletal deformation drives changes in pore pressure. The negative sign indicates that volumetric expansion (positive $\mathbf{k} \cdot \hat{\mathbf{u}}$) reduces the pore pressure, consistent with physical expectations. The frequency dependence of $B(s)$ reveals that this coupling strengthens with increasing growth rate, making high-frequency modes more susceptible to hydromechanical interaction. As a consequence, this frequency-dependent coupling induces the rich spectral structure observed in coupled poroelastic systems.

2.4. Coupled Spectral System and Dispersion Relations.

The complete spectral analysis emerges by combining the transformed momentum and mass balance equations into a unified block system. This coupling reveals the fundamental dispersion characteristics that govern wave propagation, instability growth, and the transition between stable and unstable regimes in saturated geomaterials.

Block Matrix Formulation. Combining equations (23) and (26), the coupled spectral system assumes the block matrix form:

$$\begin{bmatrix} \mathbf{Q}(\mathbf{k}) & -i\chi\mathbf{k} \\ iB(s)\mathbf{k}^{\mathsf{T}} & A(\mathbf{k},s) \end{bmatrix} \begin{bmatrix} \hat{\mathbf{u}} \\ \hat{p} \end{bmatrix} = \mathbf{0}. \tag{32}$$

This matrix structure encapsulates the hydromechanical coupling. The diagonal blocks represent the individual mechanical ($\mathbf{Q}(\mathbf{k})$) and hydraulic ($A(\mathbf{k},s)$) responses, while the off-diagonal terms encode the bidirectional coupling through Biot's coefficient χ and the storage-dependent term $B(s)$.

Remark 1. *The block structure reveals fundamental asymmetries in the coupling mechanism. The mechanical-to-hydraulic coupling (upper-right block) depends only on the wave vector* $\mathbf{k}$*, reflecting the instantaneous effect of volumetric strain on pore pressure. In contrast, the hydraulic-to-mechanical coupling (lower-left block) involves the growth rate* s*, indicating that pressure-induced mechanical responses depend on the time scale of the perturbation that triggers the coupling.*

Dispersion Relation Derivation. Nontrivial solutions to the homogeneous system (32) require the determinant to vanish:

$$\det \begin{bmatrix} \mathbf{Q}(\mathbf{k}) & -i\chi\mathbf{k} \\ i\,B(s)\mathbf{k}^{\mathsf{T}} & A(\mathbf{k},s) \end{bmatrix} = 0. \tag{33}$$

Expanding this determinant using the block structure we obtain:

$$A(\mathbf{k},s)\det(\mathbf{Q}(\mathbf{k})) - \chi B(s)\mathbf{k}^{\mathsf{T}}\mathbf{Q}^{-1}(\mathbf{k})\mathbf{k}\det(\mathbf{Q}(\mathbf{k})) = 0. \tag{34}$$

Assuming the acoustic tensor remains invertible (i.e., $\det(\mathbf{Q}(\mathbf{k})) \neq 0$), we can divide through and rearrange terms using the definitions from (26). Substituting the expressions for $A(\mathbf{k},s)$ and $B(s)$, yields:

$$\left[M_0 + S_0\chi\mathbf{k}^{\mathsf{T}}\mathbf{Q}^{-1}(\mathbf{k})\mathbf{k}\right]s + \Pi_0 + A_{\text{diff}}(\mathbf{k}) - i\,A_{\text{phase}}(\mathbf{k}) = 0. \tag{35}$$

Solving for the growth rate s gives the fundamental dispersion relation:

$$\boxed{s(\mathbf{k}) = -\frac{\Pi_0 + A_{\text{diff}}(\mathbf{k}) - i\,A_{\text{phase}}(\mathbf{k})}{M_0 + S_0\chi\mathbf{k}^{\mathsf{T}}\mathbf{Q}^{-1}(\mathbf{k})\mathbf{k}}} \tag{36}$$

This compact expression encodes the spectral response of the coupled hydromechanical system, serving as the foundation for understanding stability, wave propagation, and localization phenomena.

Physical Interpretation of the Dispersion Relation. The dispersion relation (36) reveals many physical insights. The numerator combines reactive effects (Π_0), diffusive stabilization ($A_{\text{diff}}(\mathbf{k})$), and phase-drift contributions ($A_{\text{phase}}(\mathbf{k})$), representing the driving forces for perturbation growth or decay.

The denominator introduces a modified storage coefficient:

$$\mathcal{D}(\mathbf{k}) = M_0 + S_0\chi\mathbf{k}^{\mathsf{T}}\mathbf{Q}^{-1}(\mathbf{k})\mathbf{k}, \tag{37}$$

which governs the effective time scale of the coupled response. This modified storage combines the baseline fluid storage M_0 and a mechanical contribution proportional to the inverse acoustic tensor. The mechanical contribution becomes significant when the acoustic tensor approaches a singularity, indicating proximity to mechanical instability. The term $\mathbf{k}^{\mathsf{T}}\mathbf{Q}^{-1}(\mathbf{k})\mathbf{k}$ represents the mechanical compliance in the direction of wave propagation. Large values indicate directions where the material offers little resistance to deformation, potentially leading to preferred orientations of localization.

Stability Analysis. The stability of the coupled system depends on the real part of the growth rate remaining non-positive for all wave vectors. This restriction implies the following constraint:

$$\Re[s(\mathbf{k})] = -\frac{A_{\text{diff}}(\mathbf{k}) + \Pi_0}{M_0 + S_0\chi\mathbf{k}^{\mathsf{T}}\mathbf{Q}^{-1}(\mathbf{k})\mathbf{k}} \leq 0 \quad \forall\mathbf{k} \neq \mathbf{0}. \tag{38}$$

Since $A_{\text{diff}}(\mathbf{k}) = \mathbf{k}\cdot\mathbf{C}_{w0}\cdot\mathbf{k} \geq 0$ always provides stabilization, the critical factor becomes the competition between the diffusive damping and the reactive destabilization governed by Π_0. The modified storage coefficient in the denominator $\mathcal{D}(\mathbf{k})$ determines the solution stability. This discriminant defines a storage coefficient, allowing us to distinguish between physical and singular information propagation. When $\mathcal{D}(\mathbf{k}) > 0$, the system exhibits conventional behavior where diffusion stabilizes short wavelengths. However, as the acoustic tensor approaches singularity (indicating mechanical instability), $\mathcal{D}(\mathbf{k})$ can become negative for certain wave directions, fundamentally altering the stability landscape.

Critical Wavelength and Localization. The dispersion relation reveals characteristic length scales that govern localization phenomena. The competition between diffusive stabilization and mechanical destabilization determines a critical wavelength λ_c below which perturbations decay and above which they may grow. For hydrostatic background conditions where $A_{\text{phase}}(\mathbf{k}) = 0$, the system exhibits purely real eigenvalues, leading to monotonic growth or decay without perturbing oscillation. When the modified storage coefficient remains positive, the transition between stable and unstable regimes occurs when:

$$A_{\text{diff}}(\mathbf{k}) + \Pi_0 = 0, \tag{39}$$

defining the neutral stability curve in wavenumber space.

Remark 2. *The system's anisotropy (i.e., the anisotropy of the acoustic tensor* $\mathbf{Q}(\mathbf{k})$ *and the hydraulic conductivity* $\mathbf{C}_{w0}$*) creates preferential directions for instability development. For example, compounding effects occur when weak directions in the acoustic tensor (near-singular eigenvectors) align with low hydraulic conductivity to produce highly localized failure modes with characteristic orientations determined by the material's fabric and loading history.*

Implications for Multiscale Behavior. Short wavelengths experience strong diffusive damping and remain stable, corresponding to grain-scale fluctuations that average out over larger volumes. Intermediate wavelengths may become unstable, leading to localization phenomena such as shear bands or compaction bands. Long wavelengths approach the limit where mechanical and hydraulic responses decouple, with the mechanical response dominated by the acoustic tensor properties and the hydraulic response governed by large-scale pressure gradients. This scale separation underlies the effectiveness of continuum approaches for problems involving length scales much larger than the characteristic diffusion length. The rich spectral structure revealed by the dispersion relation allows our analysis framework to bridge microscale material behavior with macroscale failure patterns, providing a theoretical foundation for understanding how localized instabilities emerge from distributed loading in saturated geomaterials under general drainage conditions.

System Response and Stability Implications. The pressure operator decomposition (27) also offers physical insight into the system's behavior. Stability requires that the real part of $A(\mathbf{k}, s)$ remains positive for all physically relevant wave numbers. The diffusive term $A_{\text{diff}}(\mathbf{k})$ always contributes a positive real part, providing stabilization. However, the reactive term $A_{\text{react}}(s)$ can become negative for sufficiently large growth rates or unfavorable background conditions, potentially triggering instability.

The phase-drift term introduces complex dynamics into what might otherwise be straightforward diffusive behavior. When pressure gradients deviate from hydrostatic equilibrium—whether through active loading, gravitational effects, or pre-existing stress fields—this term generates imaginary components in the growth rate that fundamentally alter the system's spectral character. Rather than simple exponential growth or decay, perturbations can now exhibit oscillatory behavior, with frequencies that depend directly on the magnitude and direction of the background pressure gradient. These oscillations create resonances where mechanical instabilities can couple with hydraulic pressure waves, potentially amplifying disturbances that would otherwise decay. The stability boundaries in the complex s-plane no longer follow simple real-axis criteria but instead trace curved paths that depend on the loading history and material state. When phase-drift effects become significant, predicting the onset of instability requires tracking both the amplitude growth rates and the phase relationships between mechanical and hydraulic perturbations. This spectral framework exposes the intricate choreography between competing physical processes in fully and partially saturated tailings. Storage mechanisms determine how quickly the system can respond to perturbations. Diffusion provides the primary stabilizing force, spreading pressure disturbances across space and time. Advective transport, captured by the phase-drift terms, can either enhance or disrupt this stabilization depending on the flow direction relative to the instability pattern. Hydromechanical coupling directly links these hydraulic processes to mechanical deformation, creating feedback loops that can either dampen or amplify growing instabilities.

3. One-Dimensional Spectral Reduction

The one-dimensional reduction can improve the understanding of the fundamental mechanisms governing coupled hydromechanical stability while eliminating geometric complexities that can obscure the underlying physics. This reduction allows us to discuss in detail the essential competition between diffusive stabilization and mechanical softening, establishing the theoretical foundation for understanding localization in more complex geometries.

3.1. **Simplified Dispersion Relation.** For longitudinal perturbations along the volumetric direction with wave vector $\mathbf{k} = k\mathbf{e}_v$, the three-dimensional dispersion relation (36) reduces to a scalar form. The acoustic tensor simplifies to $\mathbf{Q}(k\mathbf{e}_v) = k^2 E_{ep}$, where E_{ep} represents the volumetric one-dimensional elastoplastic tangent modulus. Within the flow-liquefaction context, we interpret the elastoplastic tangent modulus as a component that defines the material's compressibility. Alternatively, the diffusion term becomes $A_{\text{diff}}(k) = C_{w0}k^2$, where C_{w0} is the scalar hydraulic conductivity in the volumetric direction. The one-dimensional dispersion relation thus takes the form:

$$s(k) = -\frac{\Pi_0 + C_{w0}k^2 - iS_pC'_w(\partial_x p_0 + \rho_w g_x)k}{M_0 + {}^{\chi\, S_0}\!/_{E_{ep}}}, \tag{40}$$

capturing the one-dimensional spectral response, including reactive contributions (Π_0), diffusive stabilization ($C_{w0}k^2$), phase-drift effects (the imaginary term), and the modified storage coefficient in the denominator ($\mathcal{D} = M_0 + {}^{\chi\, S_0}\!/_{E_{ep}}$).

Physical Interpretation of the One-Dimensional Response. The modified storage coefficient fundamentally couples the hydraulic and mechanical responses. The baseline fluid storage M_0 combines with a mechanical contribution $\chi S_0/E_{ep}$ that depends on the elastoplastic volumetric tangent modulus. When E_{ep} becomes small (more compressible material), this mechanical contribution grows large, altering the effective storage characteristics. The numerator structure shows how different physical mechanisms compete to drive stability or instability. The diffusive term $C_{w0}k^2$ always provides stabilization proportional to k^2, favoring the decay of short-wavelength perturbations. The reactive term Π_0 can either stabilize or destabilize depending on the background loading history and material nonlinearity. The phase-drift term $S_pC'_w(\partial_x p_0 + \rho_w g_x)k$ introduces complexity through its dependence on the deviation from hydrostatic equilibrium. This term scales linearly with wave number, creating a different wavelength dependence than the quadratic diffusion term and potentially leading to preferential wavelength selection.

Hydrostatic Equilibrium and Pure Diffusion. Under hydrostatic conditions where the pressure gradient balances gravity ($\partial_x p_0 + \rho_w g_x = 0$) and with no background loading effects ($\Pi_0 = 0$), the dispersion relation reduces to its simplest form:

$$s(k) = -\frac{C_{w0}k^2}{M_0 + {}^{\chi\, S_0}\!/_{E_{ep}}} = -\frac{C_{w0}}{\mathcal{D}}k^2 = -D_{\text{eff}}k^2, \tag{41}$$

where the effective diffusion coefficient is: $D_{\text{eff}} = {}^{C_{w0}}\!/_{\mathcal{D}}$. This reduction to pure diffusive behavior reveals the classical parabolic character of coupled poroelastic systems under equilibrium conditions. All perturbations decay exponentially with a rate proportional to k^2, characteristic of diffusion-dominated processes. The effective diffusion coefficient D_{eff} encodes the complete hydromechanical coupling. Unlike simple thermal or chemical diffusion, this coefficient depends on both hydraulic properties (C_{w0}) and mechanical response characteristics through the modified storage term in the denominator.

Stability Analysis and Strain Softening. The stability condition requires $\Re[s(k)] \leq 0$ for all wave numbers $k \neq 0$. Under hydrostatic conditions, this reduces to:

$$D_{\text{eff}} = \frac{C_{w0}}{\mathcal{D}} \geq 0. \tag{42}$$

Since $C_{w0} > 0$ always, stability depends entirely on the sign of the denominator $\mathcal{D} = M_0 + \chi\, S_0/E_{ep}$. The system remains stable as long as:

$$\mathcal{D} = M_0 + \frac{\chi\, S_0}{E_{ep}} > 0 \quad \Rightarrow \quad |E_{ep}| > \frac{\chi\, S_0}{M_0}. \tag{43}$$

This inequality establishes a critical threshold for volumetric compressibility which ultimately will drive the flow-liquefaction. Mild softening can be tolerated without triggering instability, provided the hydraulic storage M_0 remains sufficiently large relative to the mechanical coupling strength χS_0.

Critical Softening and Wavelength Selection. At the stability boundary where $M_0 + {}^{\chi\, S_0}\!/_{E_{ep}} = 0$, the effective diffusion coefficient becomes infinite, indicating that the parabolic character of the governing equations breaks down. Beyond this threshold, the denominator becomes negative, which fundamentally alters the system's response. When instabilities occur, they manifest through finite-wavelength perturbations rather than short-wavelength modes. This wavelength selection arises from the competition between the stabilizing diffusion term $C_{w0}k^2$ and destabilizing contributions from background loading or mechanical coupling. The characteristic unstable wavelength depends on the specific form of the destabilizing terms determining the expected size of localization phenomena. Short-wavelength instabilities result in thin shear bands, whereas longer-wavelength instabilities produce more diffuse failure zones.

3.2. Implementation Guidelines for Numerical Stability in Fully-coupled Simulations.

The spectral analysis provides direct guidance for numerical implementation of coupled hydromechanical problems. By connecting theoretical dispersion properties to computational parameters, we establish practical criteria for sizing the time steps and the load increments, ensuring physically meaningful results while maintaining numerical stability.

Mesh-Scale Mode Suppression and Time Step Selection. The finite element discretization introduces a natural upper bound on resolvable wave numbers determined by the Nyquist criterion. For a mesh with characteristic element size h_{elem}, the largest representable wave number is:

$$k_{\max} = \frac{\pi}{h_{\text{elem}}}. \tag{44}$$

This high-frequency mode represents the finest spatial oscillation that the discretization can capture without aliasing. However, these mesh-scale modes often carry no physical significance and can contaminate the solution if allowed to persist. In hydrostatic conditions, the system exhibits pure diffusive behavior with effective diffusion coefficient D_{eff}, high-frequency perturbations decay exponentially according to:

$$|\hat{p}(k,t)| = |\hat{p}(k,0)| e^{-D_{\text{eff}}\, k^2 t}. \tag{45}$$

The characteristic decay time for the mesh-scale mode becomes:

$$\tau_{1/2}(k_{\max}) = \frac{\ln 2}{D_{\text{eff}}\, k_{\max}^2} = \frac{\ln 2 \cdot h_{\text{elem}}^2}{\pi^2 D_{\text{eff}}} = \frac{\ln 2 \cdot h_{\text{elem}}^2}{\pi^2 C_{w0}/\mathcal{D}} = \ln 2 \left(\frac{h_{\text{elem}}}{\pi}\right)^2 \frac{M_0 + \chi\, S_0/E_{ep}}{C_{w0}}. \tag{46}$$

We can ensure mesh-scale artifacts do not propagate through the discrete solution by enforcing that the decay time is much smaller than the computational time step. The condition:

$$\tau_{1/2}(k_{\max}) \ll \Delta t \tag{47}$$

guarantees that spurious high-frequency modes decay within a single time step. Herein, we propose a quantification of this requirement; therefore, we demand that the mesh-scale mode amplitude decreases to below 1/10,000 of its original size per time step (i.e., a reduction of at least 99.99%):

$$\boxed{e^{-D_{\text{eff}}(\pi/h_{\text{elem}})^2 \Delta t} = e^{\left[-(C_{w0}/(M_0 + \chi\, S_0/E_{ep}))(\pi/h_{\text{elem}})^2 \Delta t\right]} \lesssim 0.0001} \tag{48}$$

This criterion provides a direct relationship between material properties (D_{eff}), spatial discretization (h_{elem}), and temporal discretization (Δt) that ensures robust numerical performance.

3.3. Load Rate Effects and Shear Bandwidth Control.

In quasi-static coupled analyses, the temporal progression typically follows prescribed loading patterns rather than a physical time evolution. The connection between load increments and time steps becomes:

$$\Delta t = \frac{\Delta\Sigma}{r}, \tag{49}$$

where $\Delta\Sigma$ represents the applied load increment and r denotes the loading rate. Substituting this relation into the stability condition (48) and enforcing that $\Delta t > \tau_{1/2}(k_{\max})$, allows us to solve for the diffusion-induced characteristic length for the solution term with the longest wavelength:

$$\boxed{\ell_c = \sqrt{\frac{\pi^2}{\ln 2} D_{\text{eff}} \frac{\Delta\Sigma}{r}} = \sqrt{\frac{\pi^2}{\ln 2} \frac{C_{w0}}{M_0 + \chi\, S_0/E_{ep}} \frac{\Delta\Sigma}{r}}} \tag{50}$$

This scaling relation reveals how computational and physical parameters interact to determine localization characteristics. The equation establishes that the localization bandwidth depends on three key factors: the effective diffusion coefficient, the magnitude of the load increment, and the loading rate.

Physical Interpretation of Parameter Dependencies. The scaling relationship (50) provides practical insight for modeling flow-liquefaction within the fully coupled calculation framework: larger load increments $\Delta\Sigma$ lead to wider localization bands. We can physically interpret this finding since the system has more time to redistribute stresses and pressures before the next loading step. This temporal smoothing effect prevents the formation of extremely sharp gradients. Higher loading rates r produce narrower localization bands by reducing the time available for pressure redistribution between load increments. Rapid loading approaches undrained conditions where pore pressures cannot equilibrate, leading to more localized failure patterns. The effective diffusion coefficient D_{eff} captures the material's intrinsic ability to redistribute pore pressure. Higher permeability materials (larger D_{eff}) exhibit wider localization bands because pressure gradients dissipate more readily. Conversely, low-permeability materials concentrate pore pressure changes, promoting sharper localization.

Implementation Strategy and Quality Assurance. In practice, these guidelines imply several steps. Before running simulations, modelers should evaluate the attenuation condition (48) to ensure adequate suppression of mesh-scale modes. This evaluation requires estimating the effective diffusion coefficient based on material properties and current loading conditions. For problems involving strain softening where D_{eff} may vary significantly during loading, the time step criteria should be evaluated using the minimum expected diffusion coefficient to ensure conservative estimates. Similarly, adaptive time-stepping schemes should monitor the effective diffusion coefficient and adjust the time increments accordingly. The bandwidth scaling relation (50) serves both as a predictive tool for estimating localization characteristics and as a quality check for numerical results. Computed localization widths should be consistent with the theoretical prediction, providing confidence in the accuracy of the solution.

Extensions and Limitations. These guidelines apply most directly to problems exhibiting diffusion-dominated behavior under hydrostatic conditions. When significant phase-drift effects or strong background pressure gradients are present, the analysis becomes more complex, though the fundamental principles remain valid. For three-dimensional problems with anisotropic material properties, the effective diffusion coefficient becomes direction-dependent, requiring more sophisticated analysis to determine appropriate mesh and time step sizes. However, the one-dimensional insights provide valuable guidance for establishing initial estimates and understanding the underlying physics. The regularization effect depends critically on maintaining adequate coupling between mechanical and hydraulic responses. *Numerical schemes that artificially decouple these fields or use inappropriate time integration methods may not exhibit the expected mesh-independent behavior, highlighting the importance of consistent formulation throughout the computational framework.*

4. Flow-liquefaction under a fully-coupled scheme

Table 1. HSsmall parameters for liquefiable tailings.

Parameter	Unit	Value
Model	–	HSsmall
Unit weight, γ	kN/m^3	21.0
Friction angle, ϕ'	°	30
Cohesion, c'	kPa	0
Dilation angle, ψ	°	0
G_0^{ref}	MPa	40
$\gamma_{0.7}$	–	10^{-4}
E_{ur}^{ref}	MPa	75
E_{50}^{ref}	MPa	7
E_{oed}^{ref}	MPa	10
Stress dependency, m	–	0.5
Poisson's ratio, ν_{ur}	–	0.25
OCR	–	1.00
K_0^{nc}	–	–
R_{inter}	–	0.95
Permeability, k	m/s	1×10^{-8}

The numerical results we present below, spanning both laboratory-scale triaxial simulations and dam-scale TSF analyses, demonstrate the influence of hydro-mechanical coupling in flow-liquefaction modeling. Conventional uncoupled or purely mechanical approaches, long adopted in practice, are plagued by mesh sensitivity and an inability to capture the reciprocal feedback between pore pressure and deformation. By contrast, the fully coupled formulation introduces diffusion-driven stabilization, which regularizes strain localization and yields physically interpretable results across scales.

TABLE 2. Mesh-scale mode attenuation factors for varying time step sizes in coupled hydromechanical analysis (attenuation factors) computed using the stability criterion from (48) for representative material parameters: element size $h_{\text{elem}} = 0.2$ mm and effective diffusion coefficient $D_{\text{eff}} = 1.02 \times 10^{-9}\,\text{m}^2\text{s}^{-1}$). The exponential argument $-D_{\text{eff}}(\pi/h_{\text{elem}})^2\Delta t$ quantifies the decay rate of the highest frequency mode resolvable by the mesh, while the attenuation factor represents the fraction of initial amplitude remaining after one time step. Time steps of 35 s or larger achieve attenuation below 0.01%, indicating effective suppression of spurious mesh-scale oscillations and ensuring mesh-independent localization patterns. Smaller time steps enable the propagation of high-frequency artifacts (up to 28% for $\Delta t = 5$ s), leading to mesh-aligned failure bands that contaminate the physical solution.

Δt	$-D_{\text{eff}}\big(\pi/h_{\text{elem}}\big)^2\,\Delta t$	Spurious oscillations
40	-10.04	4.3×10^{-5} (0.004%)
35	-8.79	1.5×10^{-4} (0.01%)
30	-7.53	5.3×10^{-4} (0.05%)
25	-6.27	1.8×10^{-3} (0.1%)
20	-5.02	6.5×10^{-3} (0.6%)
15	-3.76	2.4×10^{-2} (2.3%)
10	-2.51	8.1×10^{-2} (8.1%)
5	-1.25	2.8×10^{-1} (28.4%)

4.1. Constitutive model, material coupling, and mesh regularization.

Constitutive model and material description. All simulations employ the Hardening Soil model with small-strain stiffness (HSsmall), a widely adopted framework in geotechnical analysis that captures the nonlinear stress–strain behavior of granular and tailings materials. The parameter set (Table 1) corresponds to a contractive tailings material prone to softening during rapid loading, calibrated to reproduce the responses of loose, saturated tailings susceptible to flow liquefaction.

The HSsmall formulation incorporates a small-strain shear stiffness G_0^{ref}, which controls the onset of stiffness degradation, and reference moduli E_{50}^{ref}, E_{oed}^{ref}, and E_{ur}^{ref} governing deviatoric stiffness, oedometric compression, and unloading–reloading, respectively. The stiffness exponent m describes stress dependency, while the strain threshold $\gamma_{0.7}$ governs small-strain decay. Yield and plastic potential surfaces are also controlled by ϕ', ψ, and the interface reduction factor R_{inter}. Finally, permeability k governs pore-pressure diffusion, making it central to the stabilizing mechanism inherent in coupled analyses.

4.2. Triaxial test.

Simulation setup. The triaxial test provides a controlled environment for examining the mesh-regularization effect predicted in Section 3.2. We simulate an isotropically consolidated undrained (CIU) specimen using a two-dimensional axisymmetric finite element model. The cylindrical sample has a radius of 5 mm, a height of 10 mm, and is discretized with uniform elements of size $h_{\text{elem}} = 0.2$ mm. Rough ends prevent radial displacement, while a prescribed vertical displacement imposes a constant axial strain rate of $\frac{1}{180}$ %/s in all cases. The loading sequence comprises three stages: (i) isotropic consolidation to $p' = 600$ kPa under drained conditions; (ii) switch to undrained mode with displacement reset; and (iii) axial straining up to $\varepsilon_y = 20\%$ under fully coupled conditions at the same load rate with impermeable boundaries. Eight fully coupled analyses were performed using time-step increments,

$$\Delta t \in \{40,\ 35,\ 30,\ 25,\ 20,\ 15,\ 10,\ 5\}\ \text{s},$$

and compared them with a reference *undrained plastic* calculation—i.e., a purely mechanical analysis where the mass balance equations are not solved, and excess pore pressures are generated directly from the constitutive undrained response rather than from transient fluid flow. Here, parameters presented

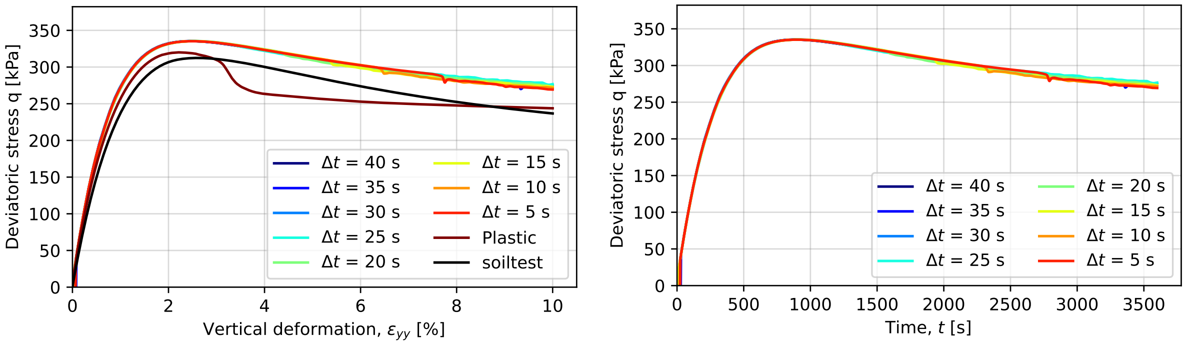

FIGURE 1. Stress–strain response from fully coupled triaxial tests. Deviatoric stress versus axial strain (left) & time (right). All curves converge onto a common envelope, confirming mesh-independent behavior and reproducing a shape similar to that obtained from a single-point calculation (soil test). Plastic calculations lead to mesh dependency.

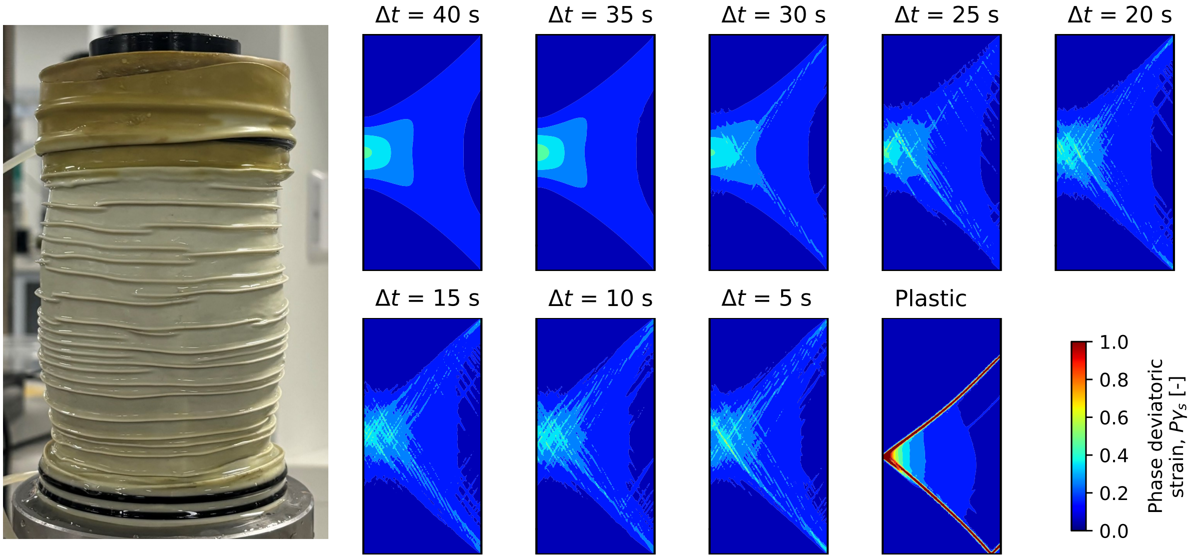

(A) Diffuse barrel-shaped failure of loose tailings.

(B) Shear strain contours for an undrained triaxial test.

FIGURE 2. Shear-band formation in fully coupled triaxial tests compared with a sampled test at the laboratory: critical role of time step filtering in localization patterns. Deformation fields at $\varepsilon_{yy} = 20\%$ reveal distinct morphological transitions controlled by the temporal discretization parameter Δt. For time steps exceeding 35 s, the system develops larger wavelength solutions, whereas smaller time increments ($\Delta t < 35$ s) produce spurious multiple bands aligned with the finite element mesh, representing unresolved short-wavelength perturbations that contaminate the physical solution.

in Table 1 were used to compute the effective diffusion coefficient, and a fully saturated material with a permeability of 1×10^{-12} m/s, obtaining a final value of $D_{\text{eff}} = 1.02 \times 10^{-9}\,\text{m}^2\text{s}^{-1}$. Table 2 reports the predicted attenuation factors, computed using (48). Since, the finite element mesh imposes a maximum resolvable wavenumber $k_{\max} = \pi/h_{\text{elem}}$, beyond which high-frequency modes become non-physical and can corrupt the solution. These mesh-scale perturbations decay exponentially with a characteristic time $\tau_{1/2}(k_{\max}) \propto h^2_{\text{elem}}/D_{\text{eff}}$, governed by the effective diffusion coefficient. Thus, we suppress these spurious oscillations by limiting the time step Δt to be $e^{-D_{\text{eff}}(\pi/h_{\text{elem}})^2\Delta t} \lesssim 0.0001$, ensuring that nonphysical modes decay by at least 99.99% within one step.

Figures 1–3 summarize the numerical results of the triaxial tests. Stress–strain curves collapse onto a single envelope for a fully coupled scheme, following a similar pattern shown by a single point simulation (soil test), whereas uncoupled (plastic) calculation leads to an early softening response and the emergence of element-scale shear bands on top of larger wave-length solutions which drives the typical barrel-shaped

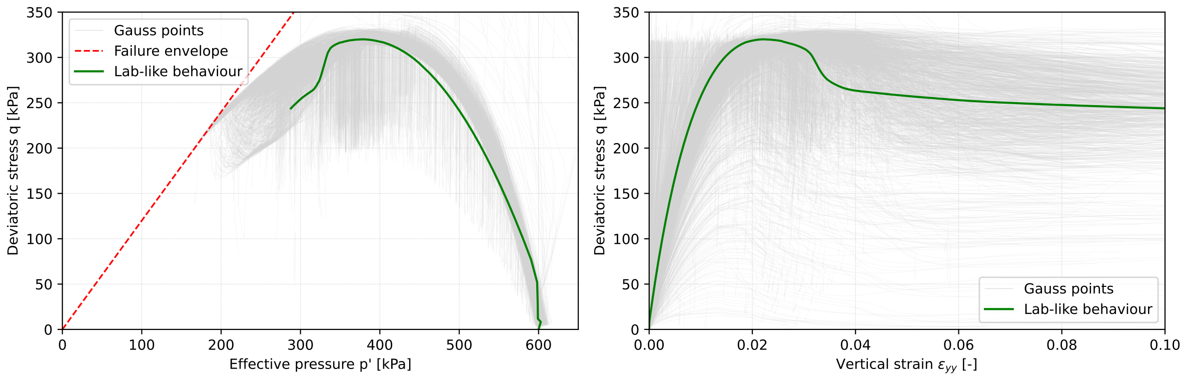

(A) Uncoupled plastic calculation. Gauss-point trajectories scatter broadly around the bulk response, with many overshooting the failure envelope before softening. Unloading paths are frequent, signaling bifurcation and severe localization. Local peak deviatoric stresses approach ≈ 330 kPa, exceeding the averaged maximum of ≈ 310 kPa. The $q-\varepsilon_y$ curve shows similar divergence: while the averaged response peaks at $\varepsilon_y \approx 0.02$, individual points follow disparate paths, some softening rapidly while others continue straining almost elastically.

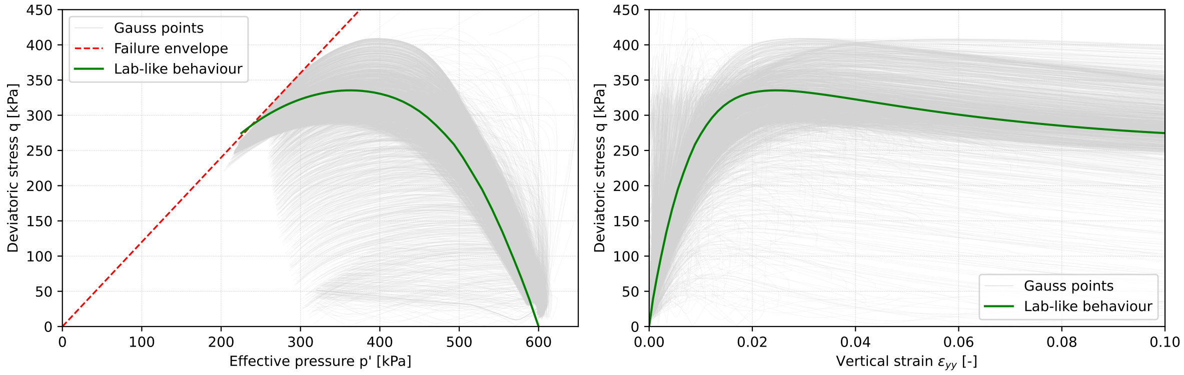

(B) Fully coupled calculation with $\Delta t = 40$ s. The $q-p$ scatter contracts around the bulk curve, and unloading trajectories nearly vanish. Diffusion redistributes stresses, suppresses local overstressing, and promotes uniform energy dissipation across the specimen. In $q-\varepsilon_y$ space, the scatter narrows, with the averaged curve bounding nearly all Gauss-point responses. The outcome is a smoother, mesh-independent, and rate-insensitive softening branch. Time-step size enforcement suppresses local overstressing and avoids unphysical responses.

FIGURE 3. Stress–strain paths at Gauss points vs averaged specimen response

failure in loose tailings (see Figure 2 (a) and (b)). Yet, even in cases where lower-wavelength shear bands are propagated, the global stress-strain behavior remains within engineering tolerance, albeit with evident mesh sensitivity due to the dominance of the larger-wavelength solutions in the solution.

Local versus global behavior. Figure 3 contrasts the global specimen response and Gauss-point stress paths. In the uncoupled plastic calculation, integration points scatter broadly, with many overshooting the failure envelope before softening, thereby producing unloading paths and bifurcation signatures. During softening, points outside the shear band begin to unload elastically. Because of the imposed undrained condition ($\varepsilon_v = 0$) the mean effective pressure remains constant during unloading, and the stress path drops vertically in the q-p plane as shear stress decreases. Local peak deviatoric stresses approach ≈ 330 kPa, even as the averaged curve peaks nearer ≈ 310 kPa. Similarly, while the global $q-\varepsilon_y$ curve peaks around $\varepsilon_y \approx 0.02$, individual Gauss points follow divergent paths, with some softening rapidly and others straining almost elastically. Severe localization is thus hidden beneath the smooth green envelope. With full coupling and $\Delta t = 40$ s, the picture changes. The $q-p$ scatter contracts around the bulk curve, unloading trajectories nearly vanish, and energy dissipation is distributed more uniformly. The $q-\varepsilon_y$ scatter also narrows, with the averaged curve bounding nearly all point responses. Diffusion suppresses local overstressing, aligning microscopic and macroscopic behavior. The outcome is a smoother, mesh-independent, rate-insensitive softening branch.

Interpretation & broader perspective. Together, these results show that coupling momentum and mass balance equations regularizes the softening response. Pore-pressure diffusion acts as an implicit

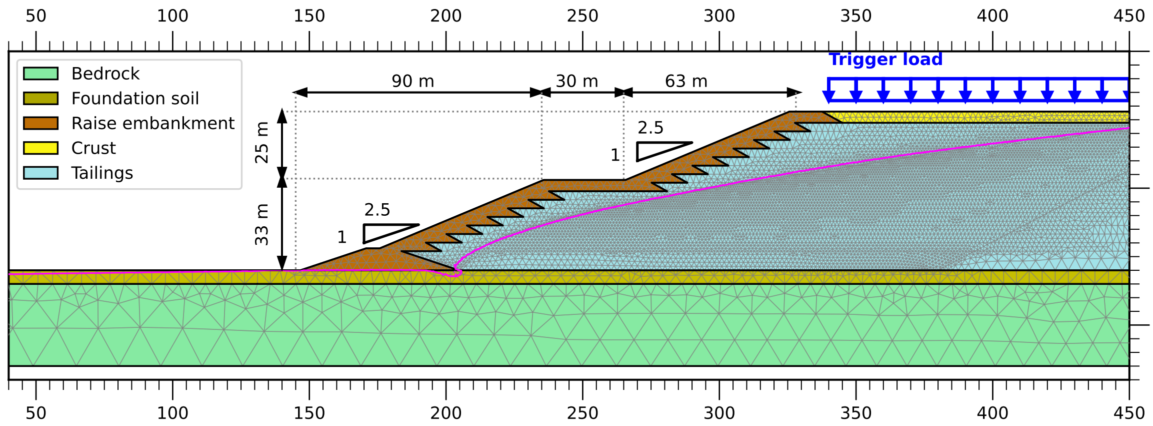

FIGURE 4. Geometry of the upstream-raised TSF model and trigger load.

viscous-like mechanism, resisting abrupt volumetric changes, damping high-frequency perturbations, and imposing a finite localization width. When the time step is sufficiently large, this filtering dominates, thereby avoiding mesh-dependent solutions. For very small time-step increments, unresolved modes survive, shear bands fragment, and mesh dependence dominates the shear contours.

Remark 3. Shear-band morphology. *Localization patterns at* $\varepsilon_{yy} = 20\%$ *(Figure 2) reveal the spatial expression of this filtering. For* $\Delta t > 35$ *s, deformation organizes into a single barrel-shaped shear band, in agreement with experimental triaxial tests for loose tailings samples. For smaller increments, multiple element-aligned bands appear, a direct manifestation of unresolved short-wavelength perturbations. Interpreted through the morphing-pattern framework (Regenauer-Lieb et al., 2025a,b), the distinction reflects whether the system locks onto a dominant wavelength or permits the coexistence of competing instabilities. At the limit case of an uncoupled plastic calculation, a unique shear band is propagated, which does not correspond with the experimental evidence for loose tailings undergoing flow-liquefaction.*

Seen through the lens of morphing patterns, the triaxial results embody a universal instability mechanism. Strong attenuation favors the selection of a single coherent shear band—a stable morphology. Weak attenuation allows multiple short bands, reflecting the competition of unstable modes. This mirrors Turing-type instabilities, where emergent wavelength depends on the balance of local amplification and diffusion. The triaxial test thus goes beyond validating a numerical criterion: it illustrates how hydro-mechanical coupling shapes the geometry of failure, linking internal diffusion with external loading to produce physically consistent localization patterns in geomaterials.

4.3. **TSF flow-liquefaction analysis.**

The second set of analyses extends the study from the element scale to the field scale, focusing on the vulnerability of a Tailings Storage Facility (TSF) to flow liquefaction. The framework follows the methodology (Ledesma et al., 2022) and adopts the representative configuration proposed by (Tasso et al., 2024). Figure 4 shows the model geometry, principal geotechnical units, and trigger load considered for the assessment. The geometry corresponds to a hypothetical upstream-raised TSF with a total height of 58 m, a mid-height berm, and overall slope gradients of 1V : 2.5H. The stratigraphy includes foundation soils, embankment material, and contractive tailings, underlain by bedrock. Average mesh size on materials prone to fail, i.e. tailings and embankments, is $h_{\text{elem}} \approx 0.75$ m.

We simulate the construction in staged raises of 3.0 m at a rise rate of 2.0 m/year. This staged procedure is crucial for reproducing the stress redistribution and pore-pressure evolution that govern the in-situ state before triggering. Unlike simplified monotonic loading schemes, staged construction generates a non-uniform stress field and establishes a realistic phreatic surface position, both of which strongly influence liquefaction susceptibility. The fully coupled hydro-mechanical formulation proves essential in this context. By solving simultaneously for displacements and pore pressure, the scheme captures the competition between deformation, staged construction effects, and pore-pressure diffusion. In particular, it enables assessment of partially drained triggers, where the hydraulic conductivity of the tailings dictates whether loading conditions lead to drained, partially drained, or undrained behavior.

4.4. **Influence of load rate r on localization bandwidth.**

The external load rate r plays a decisive role in governing the competition between hydraulic diffusion and mechanical softening. In fully coupled

TABLE 3. Parametric sweep on external load rate r influence on liquefaction triggering. Columns report: applied load rate, failure time t_f, numerical time-step size Δt, imposed load increment $\Delta\Sigma$, predicted trigger load, and dimensionless velocity. For extremely slow rates ($r \leq 2 \times 10^{-7}\,$kPa/s), diffusion keeps pace with loading, leading to near-drained behavior. Failure times extend to several years ($t_f \sim 10^{10}$ s), and the system resists liquefaction until very high stresses ($\gtrsim$ 1100 kPa). As r increases, pore-pressure diffusion lags progressively behind loading, shortening t_f and reducing the trigger load. This trend continues until a plateau emerges for $r \geq 0.2\,$kPa/s, where further rate increases no longer affect the response. Thus, the system converges to the undrained limit, with triggering loads stabilizing around 150 kPa. The intermediate line in the table represents a transition point where the failure becomes drained-like dominated. Dimensionless velocity also converges into a fixed value on the limits, being $\sim$ 0.024 for drained and $\sim$ 0.165 for undrained.

Load rate r [kPa/s]	Failure time t_f [s]	Step size Δt [s]	Load increment $\Delta\Sigma$ [kPa]	Trigger load [kPa]	Dimensionless velocity $\ell_c^2/(t_f D_{\text{eff}})$ [-]
0.000 000 002	589 800 000 000.0	100 000 000	2	1179.6	0.024
0.000 000 02	58 979 200 000.0	10 000 000	2	1179.6	0.024
0.000 000 2	5 700 000 000.0	10 000 000	2	1140.0	0.024
0.000 002	529 688 000.0	1 000 000	2	1059.3	0.026
0.000 004	244 785 000.0	500 000	2	979.1	0.029
0.000 01	91 770 000.0	200 000	2	917.7	0.031
0.000 02	32 895 500.0	100 000	2	677.9	0.043
0.000 04	12 484 050.0	50 000	2	499.3	0.057
0.0001	3 197 380.0	20 000	2	319.7	0.089
0.0002	1 290 790.0	10 000	2	258.1	0.110
0.002	97 727.0	1000	2	195.4	0.145
0.02	8845.9	100	2	176.9	0.160
0.2	868.6	10	2	153.7	0.163
2.0	85.82	1	2	151.6	0.165
20.0	8.61	0.1	2	152.3	0.165
200.0	0.86	0.01	2	152.4	0.165

analyses, pseudo-time is defined by the applied load history, such that the increment length is

$$\Delta t = \frac{\Delta\Sigma}{r},$$

where $\Delta\Sigma$ is the prescribed load increment per step. Consequently, both $\Delta\Sigma$ and r control the effective diffusion length $\ell_c \sim \sqrt{D_{\text{eff}}\,\Delta t}$ and, by extension, the width of the shear localization zone.

Table 3 summarizes the parametric sweep. For extremely slow rates ($r \leq 2 \times 10^{-7}\,$kPa/s), the system experiences near-drained conditions: diffusion keeps pace with loading, failure times exceed several years ($t_f \sim 10^{10}\,$s), and triggering occurs at high stresses exceeding 1100 kPa. As the rate increases, drainage lags progressively behind, leading to a steady reduction in the triggering load. This trend continues until a plateau is reached near $r \geq 0.2\,$kPa/s, where further rate increases no longer alter the failure load. At this point, the response converges to the undrained limit, with triggering loads around 150 kPa.

In the other hand, the dimensionless $\ell_c^2/(t_f D_{\text{eff}}$ is also introduced, describing the type of tailings drainage during the failure. The dimensionless velocity show a value of $\sim$ 0.024 for drained triggers, shile it is increased to $\sim$ 0.165 when reach undrained behavior, with a transitioning zone in-between for partially drained triggers.

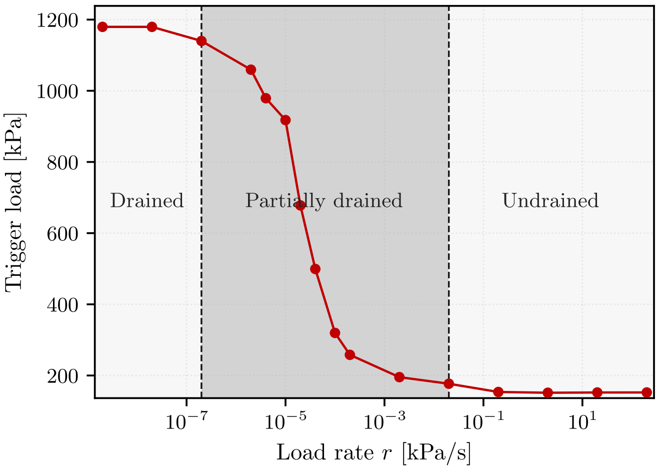

;

(A) Load rate versus trigger load.

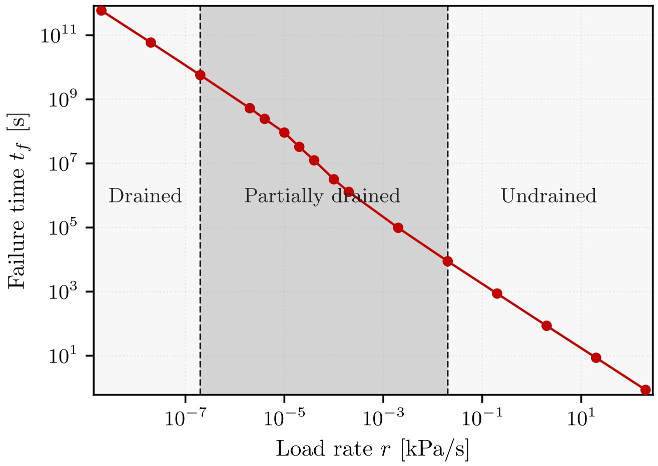

(B) Load rate versus time at failure.

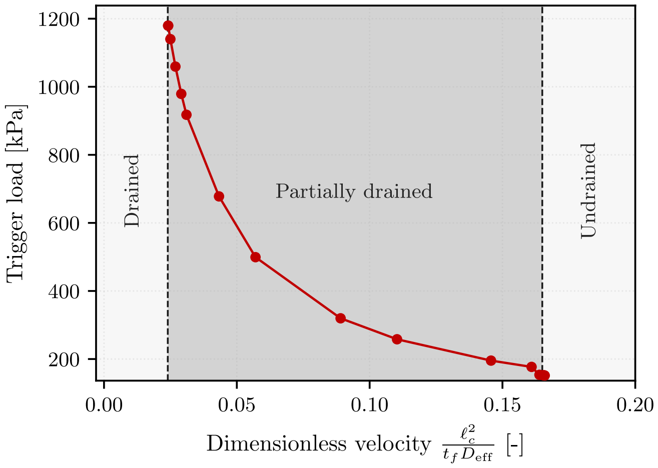

(C) Trigger load versus dimensionless velocity.

FIGURE 5. Drained-to-undrained transition as a function of the external load rate r. (a) Trigger load decreases sharply with increasing r, approaching a drained asymptote at slow rates and an undrained asymptote at fast rates. (b) Failure time follows an inverse power-law scaling, with slopes consistent with our spectral forecast of the diffusion length ℓ_c. (c) Dimensionless velocity shows a wide span for partially drained triggers, whereas it converges to fix values on the drained and undrained limits. Together, the curves demonstrate the natural rate dependence introduced by hydro-mechanical coupling: rapid loading suppresses diffusion and promotes sharp, narrow shear bands, whereas slow loading allows dissipation and broadens the localization zone.

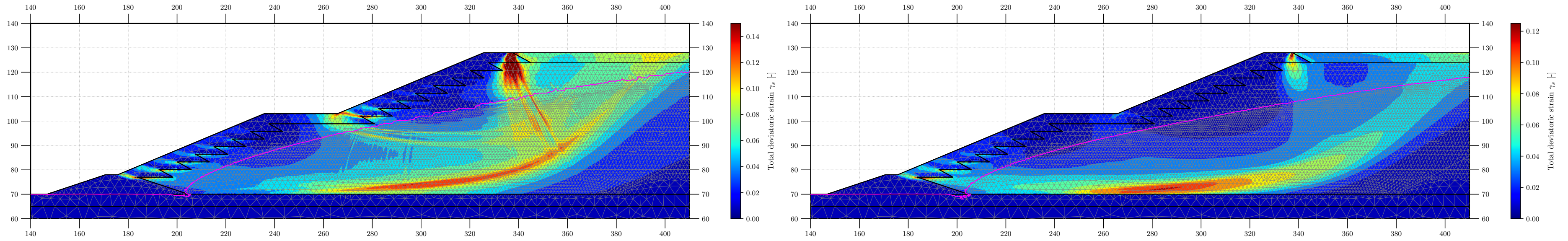

(A) Rate 1×10^{-5} kPa/s.

(B) Rate 4×10^{-5} kPa/s.

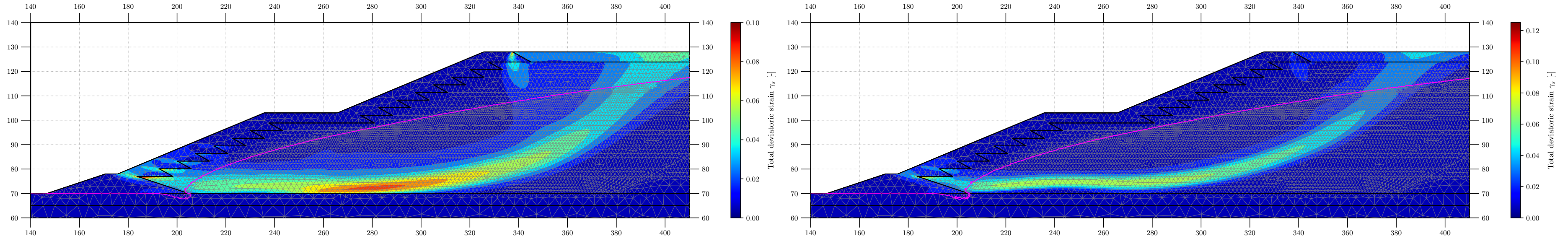

(C) Rate 1×10^{-4} kPa/s.

(D) Rate 2×10^{-3} kPa/s.

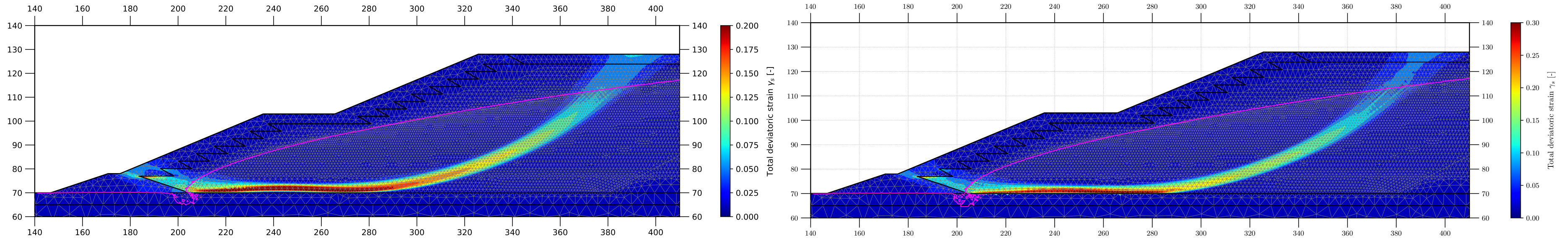

(E) Rate 2×10^{-1} kPa/s.

(F) Rate 2×10^{1} kPa/s.

Figure 6. Shear-band morphology as a function of external load rate r. At slow rates ($r \sim 10^{-5}$ kPa/s), deformation is broad and diffuse, reflecting the limit of drained-like behavior with close to continuous pore-pressure equilibration. Intermediate rates ($r \sim 10^{-5}$–10^{-3} kPa/s) yield transitional patterns: shear bands narrow, pore pressures partially accumulate, and the trigger load decreases sharply. At high rates ($r \geq 0.002$ kPa/s), localization collapses into thin, well-defined bands with concentrated pore-pressure excess, similar fully undrained responses.

Figure 5 illustrates this transition in terms of trigger load versus load rate, time at failure versus load rate, and trigger load versus dimensionless velocity. The curve of trigger load versus rate shows a sharp decline over several orders of magnitude in timescale, bounded by a drained asymptote at slow rates and an undrained asymptote at fast rates. The failure time, plotted against r, follows an inverse scaling, with log–log slopes that match the spectral predictions of ℓ_c. The dimensionless velocity shows a wide spanning for partially drained triggers, whereas on the limits its value doesn't change. These results demonstrate that hydro-mechanical coupling introduces a natural rate dependence: the faster the external load is applied, the narrower the diffusion bandwidth and the sharper the strain localization.

The deformation patterns shown in Figure 6 reinforce this interpretation. At slow rates ($r \sim 10^{-5}\,\mathrm{kPa/s}$), deformation is broad and diffuse, reflecting the limit of drained-like behavior with close to continuous pore-pressure equilibration. Intermediate rates ($r \sim 10^{-5}$–$10^{-3}\,\mathrm{kPa/s}$) produce transitional behavior: shear zones narrow down, pore pressures partially accumulate, and the trigger load drops rapidly. At high rates ($r \geq 0.2\,\mathrm{kPa/s}$), deformation collapses into thin, well-defined bands, and excess pore pressures concentrate sharply, mimicking a fully undrained response.

Taken together, these findings highlight the sensitivity of liquefaction analyses to the choice of external loading rate. In practice, this underscores the importance of relating numerical rate parameters to plausible field scenarios. Overly slow numerical rates may exaggerate stability margins by implicitly permitting drainage, while excessively fast rates may underestimate them by enforcing undrained conditions. Reliable assessments, therefore, require loading rates consistent with the expected timescales of seismic shaking, operational loading, or other relevant triggers.

Table 4. Influence of hydraulic permeability on instability trigger loads in coupled triaxial compression tests. A clear transition from partially drained to fully undrained mechanical response occurs as the permeability decreases. At $k = 10^{-8}$ m/s, the trigger load reaches 177 kPa, indicating partially drained conditions as pore pressure dissipation delays failure onset and requires higher applied stresses. As permeability decreases to 10^{-10} m/s and below, trigger loads converge to approximately 158 kPa, indicating the transition to fully undrained behavior. The asymptotic plateau for permeabilities below 10^{-10} m/s confirms that diffusive time scales are longer than loading time scales, effectively decoupling hydraulic and mechanical responses.

Permeability [m/s]	Trigger load [kPa]
1x10^{-4}	1078.78
1x10^{-6}	255.45
1x10^{-8}	176.92
1x10^{-10}	159.10
1x10^{-11}	158.21
1x10^{-12}	158.16
1x10^{-14}	158.51
1x10^{-20}	158.35

4.5. **Influence of permeability on localization bandwidth.** Permeability governs the ability of pore water to dissipate pressure during loading and, in fully coupled analyses, directly controls the internal diffusion length scale that regularizes strain localization. According to the scaling relation for ℓ_c of (50), where $D_{\text{eff}} = \dfrac{C_{w0}}{M_0 + \chi\, {}^{S_0}\!/_{E_{ep}}}$ is proportional to k/μ, higher permeabilities enlarge the diffusion length, broaden shear bands, and delay the onset of instability. Conversely, low permeabilities suppress diffusion, forcing the system towards an undrained response characterized by narrow, sharply localized deformation and rapid pore-pressure build-up.

Table 4 summarizes the trigger loads obtained for different permeabilities. The trend is clear: when permeabilities are higher than $k = 10^{-8}\,\mathrm{m/s}$, the triggering load grows to values greater than in the nearly undrained cases ($\approx 158\,\mathrm{kPa}$). However, once permeability decreases below $10^{-10}\,\mathrm{m/s}$, the response plateaus, with only minor variations in the triggering load. This asymptotic behavior confirms that below a critical permeability threshold, diffusion is too slow to affect the macroscopic response. The system behaves as fully undrained (i.e., a critical permeability threshold exists below which the system exhibits a purely undrained mechanical response, regardless of further permeability reduction, with variations of less than 1 kPa (0.6%) across a four-order-of-magnitude permeability reduction).

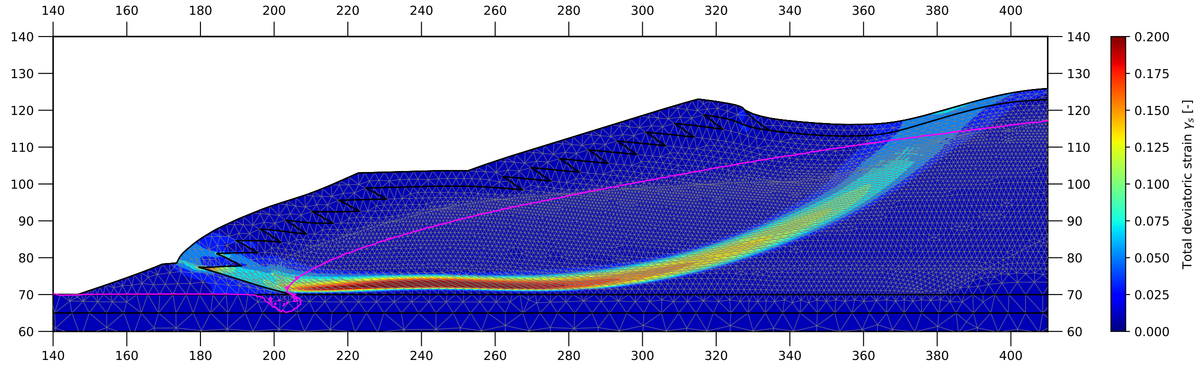

(A) Permeability $k = 1\text{x}10^{-8}$ m/s.

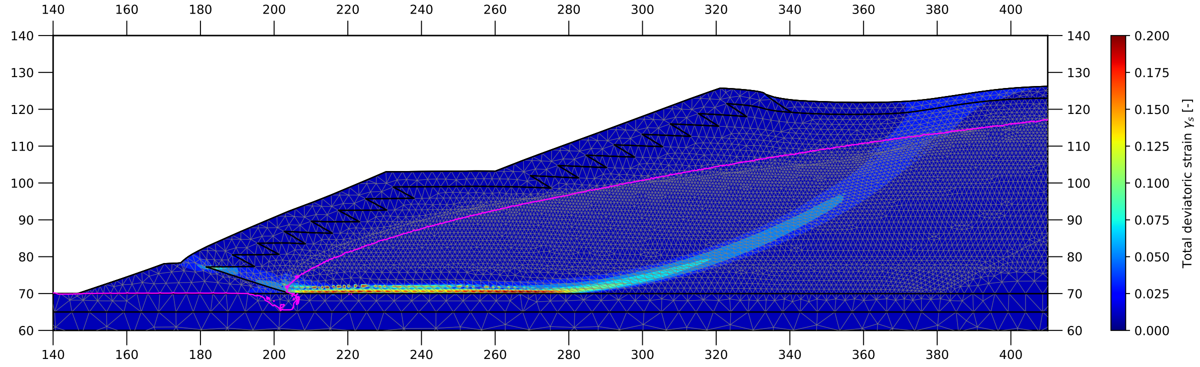

(B) Permeability $k = 1\text{x}10^{-10}$ m/s.

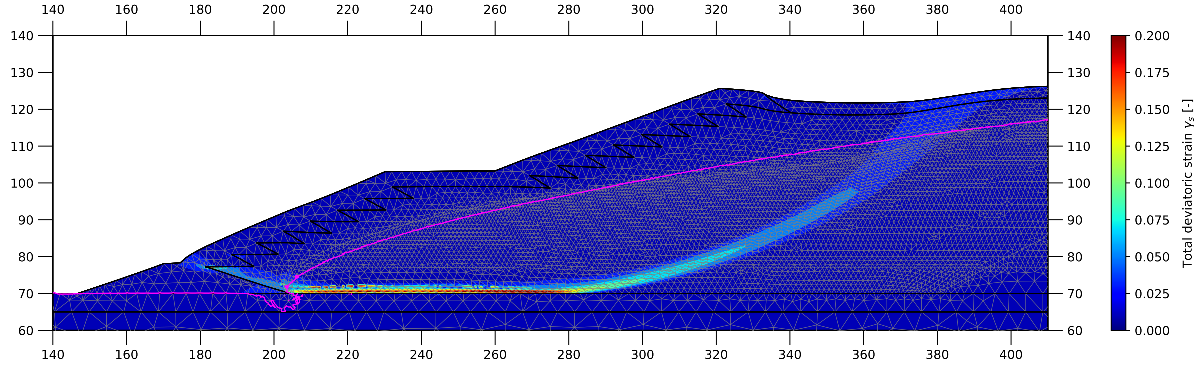

(C) Permeability $k = 1\text{x}10^{-20}$ m/s.

FIGURE 7. Influence of permeability on shear-band morphology in liquefaction. At $k = 10^{-8}$ m/s, shear localization is broad and diffuse, reflecting efficient stress redistribution through fluid flow. As permeability decreases to $k = 10^{-10}$ m/s and beyond, shear bands progressively sharpen and concentrate along critical stress trajectories, mirroring the reduced ability of the material to dissipate pore-pressure gradients. In the very low-permeability regime, deformation collapses into narrow, sharply defined zones, consistent with an undrained limit. Results show a 10× deformation magnification.

Figures 7 and 8 illustrate the associated deformation and pore-pressure fields. In higher permeability cases, shear localization is diffuse, spanning broad regions with gradual stress redistribution. As permeability decreases, bands sharpen and align along critical stress paths, with deformation concentrating into thin shear zones. At the same time, excess pore pressures intensify and become less uniformly distributed, reflecting the reduced ability of the system to dissipate hydraulic gradients. The low-k simulations highlight how the coupled formulation naturally recovers the undrained limit without requiring artificial boundary conditions or uncoupled assumptions.

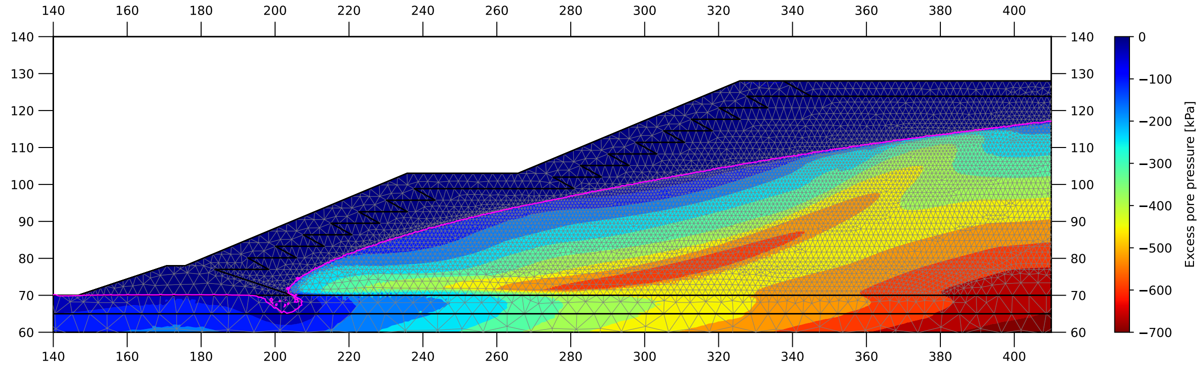

(A) Permeability $k = 1\text{x}10^{-8}$ m/s.

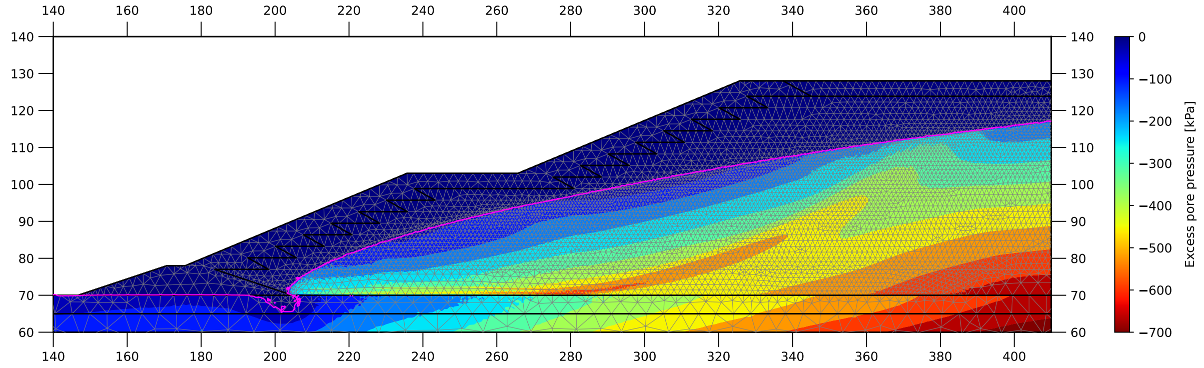

(B) Permeability $k = 1\text{x}10^{-10}$ m/s.

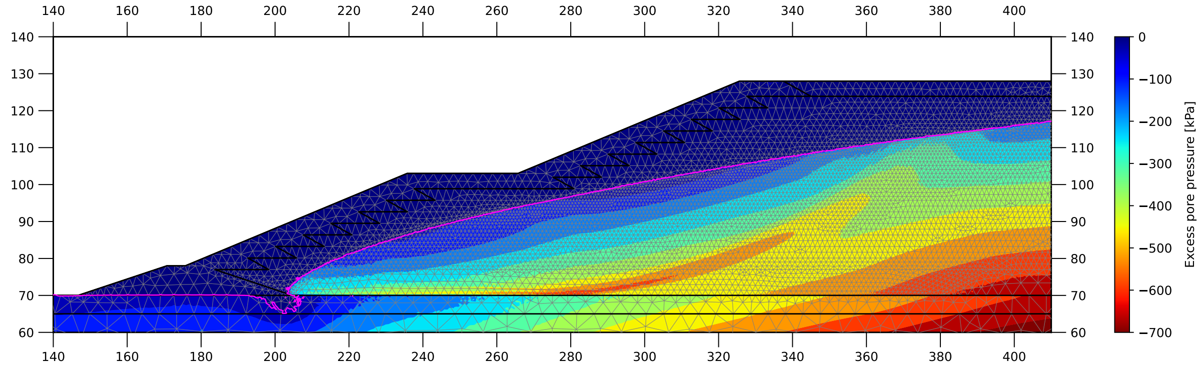

(C) Permeability $k = 1\text{x}10^{-20}$ m/s.

FIGURE 8. Influence of permeability on excess pore-water pressure at the liquefaction phase. For $k = 10^{-8}$ m/s, pore-pressure excesses remain modest and spatially diffuse, consistent with efficient hydraulic dissipation. As permeability decreases, excess pore pressures grow and concentrate into smaller zones, amplifying contractive tendencies in the tailings. At very low permeabilities, dissipation is negligible, producing sharp gradients and large pressure build-ups characteristic of fully undrained conditions.

These results demonstrate that permeability not only dictates the overall stability margin, but also the width of shear localization zones and the spatial pattern of pore-pressure excess. In practical terms, this highlights the importance of carefully characterizing the permeability of tailings materials. Small variations in k near the critical threshold can shift the response from drained-like to undrained-like, greatly altering the apparent safety margin of a TSF. Beyond this threshold, however, further decreases in k have a negligible impact on global stability, suggesting that engineering assessments should focus on the transitional range where drainage conditions are neither fully active nor fully suppressed.

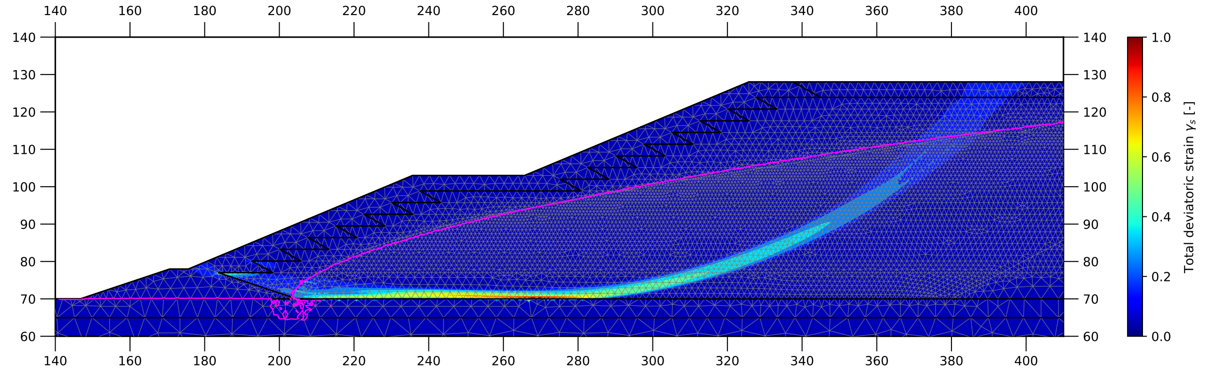

(A) Shear band - compressible material.

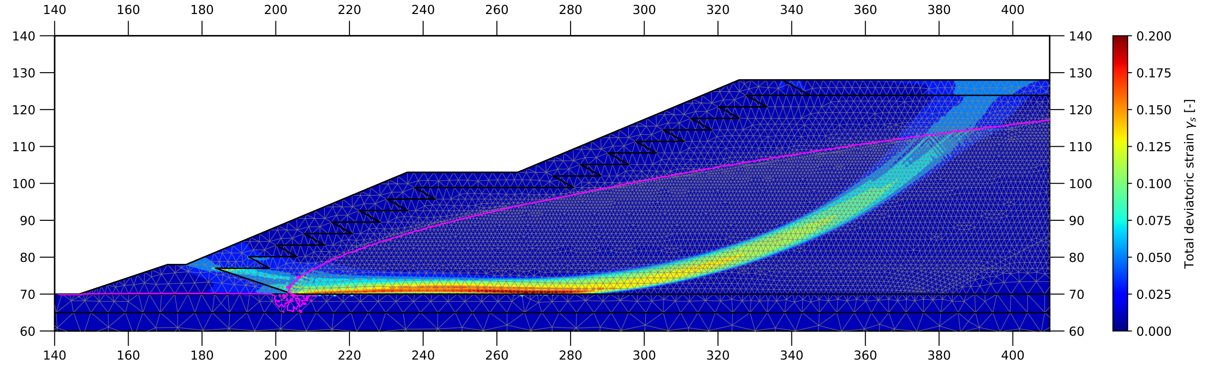

(B) Shear band - stiffer material.

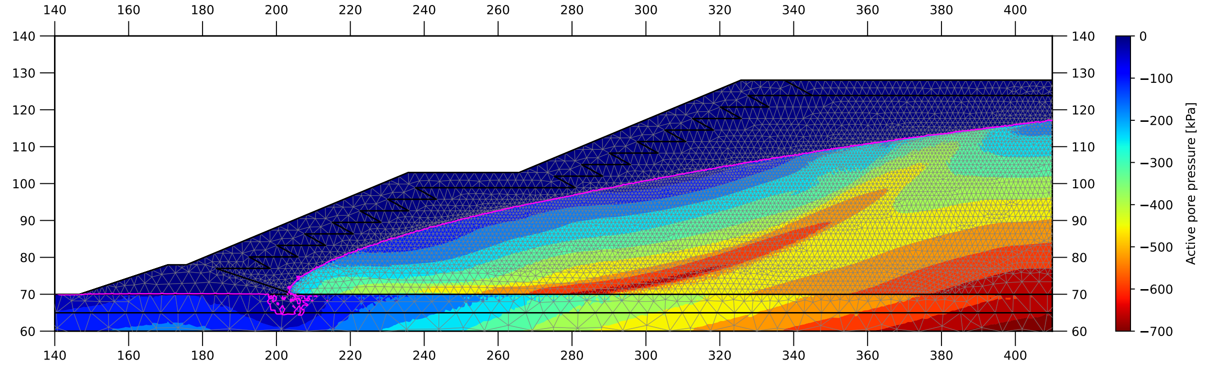

(C) Pore water pressure - compressible material.

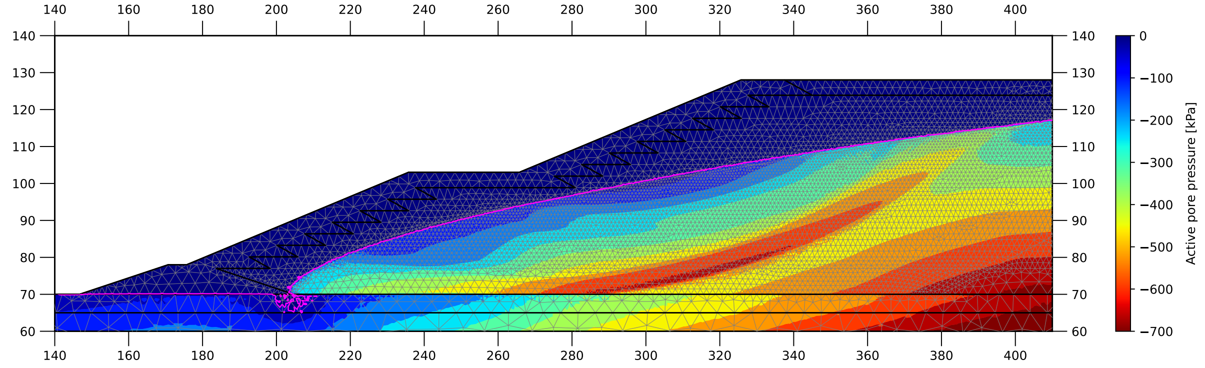

(D) Pore water pressure - stiffer material.

FIGURE 9. Material compressibility effect on the shear band morphology. Compressible materials generate pore water pressure which dissipates more slowly than stiffer materials, generating a narrower high-pressure band and, consequently, a narrower shear band.

TABLE 5. Influence of compressibility on instability trigger loads in the analysed TSF section. Results show an increase in the flow-liquefaction trigger load as the oedometric stiffness is increased, due to the lagging in pore water pressure generation.

E_{oed}^{ref} [MPa]	Trigger load [kPa]
E_{oed}^{ref} x 0.5	170.71
E_{oed}^{ref}	176.92
E_{oed}^{ref} x 2.0	210.59
E_{oed}^{ref} x 4.0	354.60

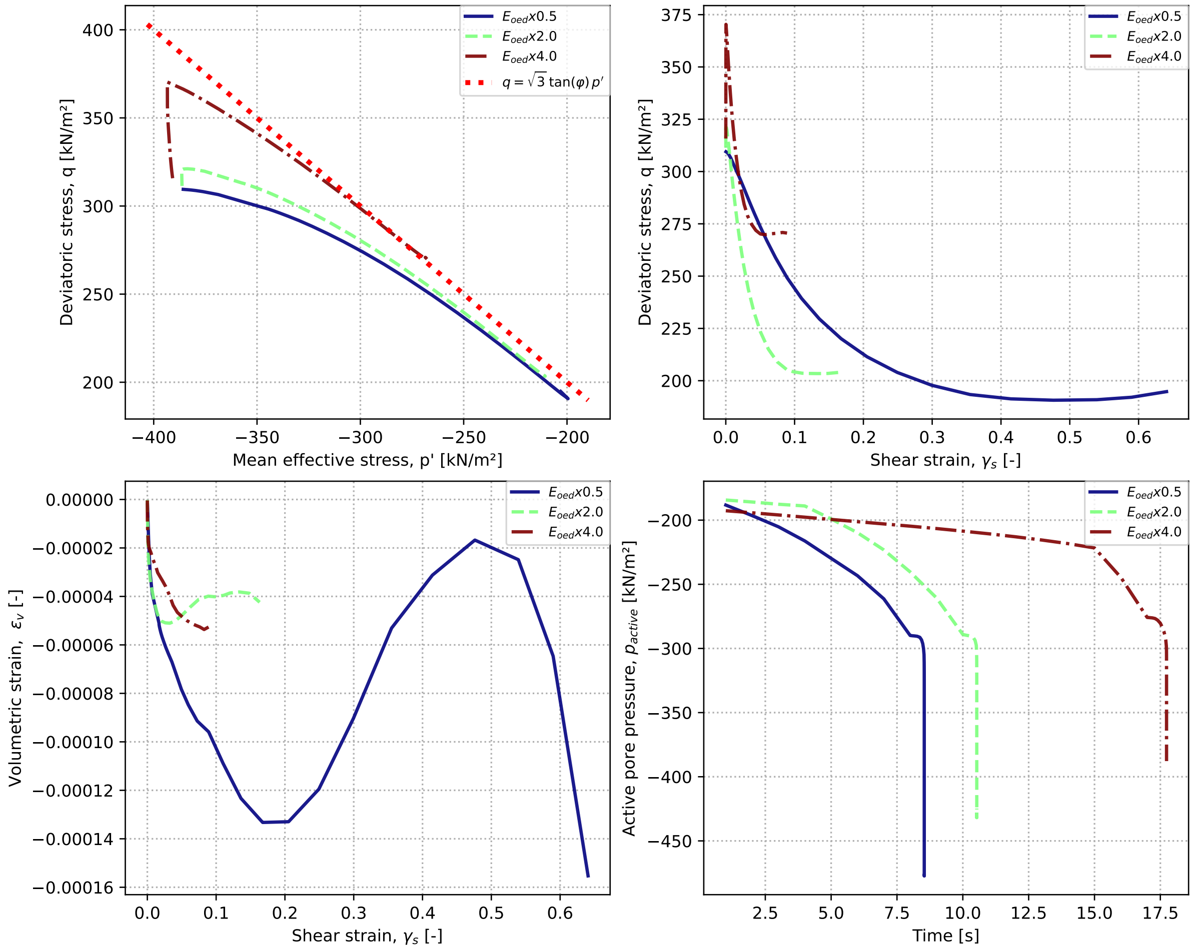

FIGURE 10. Direct shear stress path at a slip surface point for different compressibilities, throughout the triggering assessment. As the compressibility increases, the material reduces its volumetric deformation and needs more time to develop enough pore water pressure to trigger the flow-liquefaction failure. Moreover, HSsmall exhibits a strong limitation in the fully coupled context, where less compressible materials exhibit more brittle behavior; at the same time, they require higher triggering loads to develop pore water pressures and form a slip surface.

4.6. **Influence of tailings compressibility on localization bandwidth.** We seek to assess the influence of tailings compressibility on the localization bandwidth and triggering response. Thus, we scale the stiffness parameters E_{oed}^{ref}, E_{ur}^{ref}, E_{50}^{ref}, and G_0^{ref} listed in Table 1 by a common factor. This approach modifies the overall compressibility of the material while preserving its peak and residual strengths by proportionally adjusting the strains at which these occur (Sottile et al., 2020). The baseline scenario corresponds to the TSF model run at a loading rate of $r = 0.02$ kPa/s, as presented in the previous section.

Table 5 summarizes the resulting trigger loads for different oedometric stiffness values. The results show a clear trend: as stiffness increases (i.e., as compressibility decreases), the trigger load rises. This inverse relationship indicates that more compressible materials, which allow greater volumetric deformation under loading, are more susceptible to premature failure.

Figure 9 illustrates how this behavior manifests in the deformation field. Consistent with the analytical scaling relation derived in Section 3.2 for the induced shear bandwidth, the simulations show that more compressible materials form narrower and more localized shear bands, while stiffer materials distribute deformation over wider regions. The corresponding pore pressure fields follow a similar pattern: higher compressibility enhances pore-pressure accumulation within localized zones, reinforcing the link between diffusion capacity, compressibility, and the spatial extent of deformation.

Figure 10 shows the stress–strain and time-evolution data. This data is taken at a representative point along the developing slip surface. The q–p' diagram reveals that stiffer materials exhibit a pronounced initial strength increase before converging towards the direct simple shear failure line,

$$q = \sqrt{3}\,\tan\phi\, p',$$

where ϕ is the material friction angle. This initial strength gain results from reduced volumetric compressibility, as indicated by the shear strain–volumetric strain relation, which in turn delays the buildup of pore pressure during loading. The time versus pore pressure response confirms this interpretation: stiffer materials dissipate pressure gradients more effectively, whereas more compressible ones experience rapid pore-pressure rise and earlier loss of effective stress.

Remark 4. Limitations of HSsmall for Fully-Coupled Flow-Liquefaction Triggering-Load Predictions. *The shear strain–deviatoric stress response also exposes a limitation of the HSsmall model when applied to flow-liquefaction problems in a fully coupled framework. The model predicts increasingly brittle behavior for stiffer (less compressible) materials, leading to unrealistic post-peak responses inconsistent with experimental evidence (Jefferies and Been, 2016; Smith et al., 2019; Tasso et al., 2026). As a consequence, this artifact can result in artificially high trigger loads in materials that, in reality, would undergo more ductile softening and progressive failure. Therefore, while HSsmall provides valuable insight into stiffness-dependent trends, its application to brittle or highly contractive tailings should be exercised with caution, and future work should consider alternative constitutive formulations that better capture the interplay between compressibility, dilatancy, and pore-pressure generation in liquefiable materials.*

5. CONCLUSIONS

This study shows that fully coupled hydro–mechanical formulations possess an inherent, physically grounded regularization mechanism absent in purely mechanical or uncoupled models. By coupling momentum balance with pore-fluid diffusion, the governing equations naturally impose a finite localization bandwidth that limits the growth of strain-softening instabilities. This internal length scale emerges from the combined effects of material and hydraulic properties—permeability, fluid compressibility, and solid skeleton stiffness—and their interaction with the effective diffusivity and numerical parameters such as the time step, load increment, and loading rate. Together, these factors define the system's capacity to redistribute pore pressures and modulate deformation.

Numerical stability is achieved only when mesh resolution and time increments are consistent with this diffusion-driven length scale. Under such conditions, simulations yield mesh-independent predictions of both liquefaction initiation and post-trigger evolution. The spectral stability analysis establishes a clear dispersion relation governing perturbation growth: short-wavelength modes decay when the time step exceeds a critical threshold, effectively filtering out non-physical instabilities. Numerical triaxial simulations confirm this analytical prediction. For sufficiently large increments, deformation localises into single, physically consistent shear bands, and the stress–strain response became insensitive to mesh refinement. Conversely, smaller time steps permit the persistence of high-frequency modes, causing element-scale banding and premature softening. The comparison between coupled and uncoupled formulations reveals that pore-pressure diffusion plays a crucial redistributive role: it suppresses local overstressing, aligns Gauss-point stress trajectories with the macroscopic response, and ensures a smooth post-peak transition. In contrast, uncoupled models exhibit unrestrained softening and spurious unloading, resulting in non-unique and mesh-dependent outcomes.

At the tailings-storage-facility (TSF) scale, the same stabilizing mechanism governs system-wide behavior. Parametric analyses confirm that decreasing permeability systematically narrows localization bands and lowers triggering loads, driving the material response toward an asymptotic undrained regime. The coupled formulation naturally captures this transition, seamlessly linking drained, partially drained, and undrained responses without the need for artificial boundary constraints. The interaction between load rate and increment size further refines the interpretation: rapid loading accelerates pore-pressure accumulation, producing narrow, sharply defined bands, while larger increments act as diffusive filters that widen the deformation zone and damp short-wave fluctuations. This load-rate/increment-size relationship establishes a clear physical connection between hydraulic diffusivity, deformation morphology, and liquefaction susceptibility across scales.

Therefore, two major conclusions arise from these findings. First, fully coupled hydro–mechanical formulations provide a *physical*, rather than numerical, pathway to regularization. The diffusion terms embedded in the governing equations impose intrinsic length and time scales that restore uniqueness and ensure predictive reliability in liquefaction analyses. Second, they underscore the importance of numerical consistency: mesh size, time step, and load increments must respect the diffusion-controlled scales of the problem. When properly selected, these parameters enable robust, mesh-independent solutions that accurately reproduce both laboratory and field-scale behaviour. By integrating analytical insight, controlled triaxial simulations, and TSF-scale modelling, we obtain a coherent and verifiable framework for predicting liquefaction triggers and post-failure evolution. The results highlight that drained, partially drained, and undrained responses emerge not as imposed conditions but as natural outcomes of the coupled equations, governed by permeability, load rate, and boundary configuration. This unified perspective bridges theory and practice, providing a physically consistent basis for evaluating tailings dam stability and the mechanisms underlying flow liquefaction.

Future research will incorporate advanced constitutive models—particularly critical-state or anisotropic plasticity formulations—to capture progressive failure and post-liquefaction deformation more realistically. Large-scale applications should also investigate the combined influence of staged construction, hydraulic barriers, and spatial heterogeneity in permeability to assess system-wide liquefaction susceptibility. These developments would expand the predictive scope of fully coupled analyses and strengthen their integration into practical dam safety assessment and design, ensuring that the coupling between hydraulic and mechanical processes is faithfully represented across scales.

References

Z. P. Bažant and B.-H. Oh. Crack band theory for fracture of concrete. *Materials and Structures*, 16(3): 155–177, 1983. doi: 10.1007/BF02486267. URL `https://link.springer.com/article/10.1007/BF02486267`.

R. B. J. Brinkgreve, S. Kumarswamy, W. M. Swolfs, E. Engin, F. Fonseca Arévalo, N. Ragi Manoj, L. Zampich, and N. Zalamea. *PLAXIS Connect Edition V20.03 Manuals*. Bentley Systems, Delft, The Netherlands, 2020. User and Reference Manuals for PLAXIS CONNECT Edition (V20.03).

CIMNE/UPC. Computational analysis of the failure of dam i at the córrego do feijão mine (brumadinho): Final technical report. Technical report, International Centre for Numerical Methods in Engineering (CIMNE) and Universitat Politècnica de Catalunya (UPC), Barcelona, Spain, oct 2021. Final technical report submitted to the Brazilian Federal Prosecutor's Office (MPF), with independent technical oversight.

Olivier Coussy. *Poroviscoelasticity*, chapter 9, pages 261–277. John Wiley and Sons, Ltd, 2003. ISBN 9780470092712. doi: https://doi.org/10.1002/0470092718.ch9. URL `https://onlinelibrary.wiley.com/doi/abs/10.1002/0470092718.ch9`.

Wenjie Cui, Xiaotian Wu, David M. Potts, and Lidija Zdravković. Nonlocal strain regularisation for critical state models with volumetric hardening. *Computers and Geotechnics*, 157:105350, 2023. doi: 10.1016/j.compgeo.2023.105350.

G. Duvaut and J.-L. Lions. *Inequalities in Mechanics and Physics*. Grundlehren der Mathematischen Wissenschaften. Springer, Berlin, Heidelberg, 1976. ISBN 978-3-642-66165-5. doi: 10.1007/978-3-642-66165-5. URL `https://link.springer.com/book/10.1007/978-3-642-66165-5`.

Eleni Gerolymatou, Alexandros Stathas, and Ioannis Stefanou. Do multiphysics processes lead to mesh independent analyses? *International Journal of Mechanical Sciences*, 274:109265, 2024. doi: 10.1016/j.ijmecsci.2023.109265.

Michael Jefferies, Norbert R. Morgenstern, Dirk V. Van Zyl, and John Wates. Report on ntsf embankment failure, cadia valley operations, for ashurst australia. Technical report, International Centre for Numerical Methods in Engineering (CIMNE), April 2019.

Mike Jefferies and Ken Been. *Soil Liquefaction: A Critical State Approach*. CRC Press, Boca Raton, FL, 2 edition, 2016.

Milan Jirásek and Zdeněk P. Bažant. *Inelastic Analysis of Structures*. John Wiley & Sons, Chichester, 2002. ISBN 9780471987161.

Osvaldo Ledesma, Alejo Sfriso, and Diego Manzanal. Procedure for assessing the liquefaction vulnerability of tailings dams. *Computers and Geotechnics*, 144:104632, 2022.

Miguel A. Mánica, Antonio Gens, Jacques Vaunat, and Diego F. Ruiz. Nonlocal plasticity modelling of strain localisation in stiff clays. *Computers and Geotechnics*, 103:138–150, 2018. doi: 10.1016/j.compgeo.2018.07.008. URL `https://www.sciencedirect.com/science/article/pii/S0266352X18301733`.

Miguel A. Mánica, Marcos Arroyo, Antonio Gens, and Luis Monforte. Application of a critical state model to the merriespruit tailings dam failure. *Proceedings of the ICE – Geotechnical Engineering*, 175, 2021. doi: 10.1680/jgeen.21.00001.

Norbert R. Morgenstern, Steven G. Vick, and Dirk V. Van Zyl. Report on mount polley tailings storage facility breach. Technical report, Independent Expert Engineering Investigation and Review Panel, Province of British Columbia, Canada, 2015. URL `https://www.mountpolleyreviewpanel.ca/sites/default/files/report/ReportonMountPolleyTailingsStorageFacilityBreach.pdf`.

H. B. Mühlhaus and E. C. Aifantis. A variational principle for gradient plasticity. *International Journal of Solids and Structures*, 28(7):845–857, 1991. doi: 10.1016/0020-7683(91)90004-Y. URL `https://www.sciencedirect.com/science/article/pii/002076839190004Y`.

P. Perzyna. Fundamental problems in viscoplasticity. In W. Flügge and C. Truesdell, editors, *Advances in Applied Mechanics*, volume 9, pages 243–377. Academic Press, 1966. doi: 10.1016/S0065-2156(08)70009-7. URL `https://www.sciencedirect.com/science/article/pii/S0065215608700097`.

Klaus Regenauer-Lieb, Manman Hu, Qingpei Sun, Chong Liu, Zhennan Zhu, and Victor Calo. A thermodynamic framework for turing-type instabilities in deforming porous media: Part I Theory. –, 2025a. Draft. Awaiting submission.

Klaus Regenauer-Lieb, Manman Hu, Qingpei Sun, Chong Liu, Zhennan Zhu, and Victor Calo. A thermodynamic framework for turing-type instabilities in porous media: Part II Applications. –, 2025b. Draft. Awaiting submission.

F. Lopez Rivarola and N. Tasso. Evaluation of triggering of static liquefaction of tailings dams considering the swcc. *Mine Waste and Tailings Conference 2023, Brisbane, Australia*, 2023.

F. Lopez Rivarola and N. Tasso. Analysis of flow liquefaction triggering in tailings dams considering coupled flow-deformation. *Proceedings of the 17th Pan-American Conference on Soil Mechanics and Geotechnical Engineering (XVII PCSMGE), and 2nd Latin-American Regional Conference of the International Association For Engineering Geology and the Environment (IAEG), La Serena Chile*, 2024.

Laura A. Rødvand, Hans Petter Jostad, Gustav Grimstad, and Lars Andresen. Modelling mesh independent failure loads of a soft strain-softening clay using a rate dependent model. *Computers and Geotechnics*, 161:105265, 2023. PII: S0266-352X(23)002690; preprint/open version available at NTNU Open.

Erick Rógenes, Ian Torras Paes, Bruno Guimarães Delgado, Rafael Jabur Bittar, Alessandra dos Santos Gomes, Alessandro Cirone, Alomir H. Fávero Neto, and Leandro Lima Rasmussen. Assessing static liquefaction triggers in tailings dams using the critical state constitutive models CASM and NorSand. *International Journal for Numerical and Analytical Methods in Geomechanics*, 49(4):1092–1112, December 2024. ISSN 0363-9061. doi: 10.1002/nag.3914. URL `https://onlinelibrary.wiley.com/doi/10.1002/nag.3914`.

J. W. Rudnicki and J. R. Rice. Conditions for the localization of deformation in pressure-sensitive dilatant materials. *Journal of the Mechanics and Physics of Solids*, 23(6):371–394, 1975a. doi: 10.1016/0022-5096(75)90001-0. URL `https://www.sciencedirect.com/science/article/pii/0022509675900010`.

John W. Rudnicki and James R. Rice. Conditions for the localization of deformation in pressure-sensitive dilatant materials. *Journal of the Mechanics and Physics of Solids*, 23(6):371–394, 1975b. doi: 10.1016/0022-5096(75)90003-5.

Kyle Smith, Riccardo Fanni, Peter Chapman, and David Reid. Critical state testing of tailings: comparison between various tailings and implication for design. *Proceedings of Tailings and Mine Waste, Vancouver, Canada*, pages 1–12, 2019.

M. Sottile, I. Cueto, and A. Sfriso. A simplified procedure to numerically evaluate triggering of static liquefaction in upstream-raised tailings storage facilities. In *Proceedings of COBRAMSEG*, Campinas, 2020.

Mauro G. Sottile, Nicolás A. Labanda, Alejandro Kerguelén, Ignacio A. Cueto, and Alejo O. Sfriso. Stability assessment of a tailings storage facility using a non-local constitutive model accounting for anisotropic strain-softening. In Marco Barla, Alice Di Donna, and Donatella Sterpi, editors, *Challenges* *and Innovations in Geomechanics. IACMAG 2021*, volume 126 of *Lecture Notes in Civil Engineering*, pages 334–342, Cham, 2021. Springer. ISBN 978-3-030-64517-5. doi: 10.1007/978-3-030-64518-2_40. URL `https://doi.org/10.1007/978-3-030-64518-2_40`.

N. Tasso, F. Lopez Rivarola, O. De Santiago, N. Rivas, and M. Sottile. Calibration constitutive models for flow liquefaction: a word of caution. *First International Symposium of Tailings Deposits, Chihuahua, Mexico*, 2024.

Nicolas Tasso, Nicolas Labanda, Kuntan Chang, and Riccardo Fanni. Gold tailings database: parameters' variability and correlations. *Proceedings of the 21st International Conference on Soil Mechanics and Geotechnical Engineering, Vienna, Austria*, 2026. Approved. Awaiting for publication.

J. G. M. Vermeer and R. de Borst. Non-associated plasticity for soils, concrete and rock. *Heron*, 29(3):1–64, 1984. URL `https://repository.tudelft.nl/record/uuid:4ee188ab-8ce0-4df3-adf5-9010ebfaabf0`.